CHALMERS
UNIVERSITY OF TECHNOLOGY

Oxidation Behavior of FeCr Steels Interconnect in Low *p*O2 Environments of Solid Oxide Electrolysis Cells

Master of Science thesis in Materials Engineering

SWATHI KIRANMAYEE MANCHILI

THE HIGH TEMPERATURE CORROSION CENTRE
Department of Chemical and Biological Engineering
Division of Environmental Inorganic Chemistry
CHALMERS UNIVERSITY OF TECHNOLOGY
Gothenburg, Sweden 2015

Oxidation Behavior of FeCr Steels Interconnects in Low pO2 Environments of Solid Oxide Electrolysis Cells

Master of Science Thesis in Materials Engineering

60 credit points

2015

CHALMERS UNIVERSITY OF TECHNOLOGY

Supervisor: Patrik Alnegren, Jan Gustav Grolig

Examiner: Jan-Erik Svensson

ABSTRACT

The need for replacing fossil fuel energies with renewable energy sources has gained importance in the present times for economic and environmental reasons. Hydrogen is one such alternative fuel for future energy supply. Solid oxide electrolysis cells (SOEC) offer a solution for hydrogen supply in a sustainable way. Commercialization of these cells depends on the economics involved in manufacturing the components of the cells. Interconnects are used to electrically connect the cells and chromia forming ferritic stainless steels are used for such application. The interconnect materials selected for the present study, AISI 441 steel and Crofer 22 APU steel, were treated in low pO_2 atmosphere, simulating the cathode side environment of SOEC. AISI 441 steel is a commercial grade ferritic stainless steel whereas Crofer 22 APU steel was developed for interconnect application. Constant pO_2 conditions were employed but hydrogen and water vapor partial pressures were varied at 850 °C for a maximum exposure of 500 h. Environments employed were Ar-3%H_2-40%H_2O, Ar-1.5%H_2-20%H_2O and Ar-0.75%H_2-10%H_2O. Gravimetric measurements were carried out to understand oxidation kinetics. Scanning electron microscopy studies were carried out to understand the oxide scale morphology and composition. Attempts were made to evaluate area specific resistance (ASR) of oxide scale formed on Crofer 22 APU steel.

Keywords: SOEC, Ferritic stainless steels, High temperature oxidation, Interconnects

TABLE OF CONTENTS

1. INTRODUCTION 1
1.1 Background 1
1.2 Aim of the Thesis 1
1.3 Electrolysis Cells 2
1.4 Operating Principle of SOEC 2
1.5 Cell Components 4
1.5.1 Electrolyte 4
1.5.2 Electrodes 4
1.5.2.1 Cathode 4
1.5.2.2 Anode 5
1.5.3 Interconnector 5
1.5.3.1 Ceramic Interconnectors 5
1.5.3.2 Metallic Interconnectors 5
1.6 Corrosion 6
1.6.1 High Temperature Corrosion 6
1.6.2 Thermodynamics of Metal-Oxygen reactions 7
1.6.3 Kinetics 8
1.6.3.1 Logarithmic Rate Equations 9
1.6.3.2 Parabolic Rate Equation 9
1.6.3.3 Linear Rate Equation 9
1.7 Challenges Related To Interconnects: 10
1.7.1 Electrical Conductivity 10
1.7.2 Chromium Evaporation 10
2 EXPERIMENTAL TECHNIQUES AND MATERIALS 12
2.1 Materials and Preparation 12
2.2 Experimental setup 12
2.3 Characterization Techniques 13
2.3.1 Optical Microscopy (OM) 13
2.3.2 Scanning Electron Microscopy (SEM) 13
2.3.3 Electrical Characterization 14
3 RESULTS 15
3.1 Gravimetric Analysis 15
3.1.1 AISI 441 steel 15
3.1.2 Crofer 22 APU 15
3.1.3 Mass gain square Vs. Time plots 16

3.2 Microstructure Evaluation 17
3.2.1 AISI 441 Steel 18
3.2.1.1 Ar-3%H_2-40%H_2O environment 18
3.2.1.2 Ar-0.75%H_2-10%H_2O environment 19
3.2.2 Crofer 22 Steel 21
3.2.2.1 Ar-3%H_2-40%H_2O environment 21
3.2.2.2 Ar-0.75%H_2-10%H_2O environment 22
3.3 Area Specific Resistance 24
4 DISCUSSION 25
4.1 Area Specific Resistance 27
5 CONCLUSIONS 28
ACKNOWLEDGEMENTS 29
REFERENCES 30

1. INTRODUCTION

1.1 Background

One of the major challenges faced in the present times is global warming. Prime contributors to this are the greenhouse gases like CO_2, CO which, are released into the atmosphere by burning of fossil fuels. We tend to forget the fact that the fossil fuels like petroleum oil & gases are not only polluting the habitual environment but are also nonrenewable in nature. Climate change, global warming coupled with high price, drive the need to replace fossil fuels with cleaner and non-perishable sources of energy like solar energy, wind energy or hydro energy [1].

In recent times, there have been advancements in the field of renewable energy technologies whose production will have lower impact on the environment in comparison with the conventional technologies. Energy from non-renewable sources involves costly import of the raw materials like coal, petroleum apart from the establishment and maintenance costs. The costs in the production of cleaner energy involves only the establishment and maintenance costs. A major challenge involved in clean energy is the reliable supply of energy in the time and volume needed. Hydrogen is an option to store the energy generated and use it for later time. Production of hydrogen is largely by burning fossil fuels but is gradually being replaced by cleaner ways of production like electrolysis of water.

In an electrolysis process, water is split into hydrogen and oxygen with the help of electricity, and separated to avoid reformation. This hydrogen can be stored and re-electrified using fuel cells or in power gas plants whenever necessary. There is no production and emission of greenhouse gases in this process, which makes it very clean [2]. The roundabout efficiency of this process is about 30-40% but can increase to 50% if technology is efficient. Commercially, hydrogen is produced from fossil fuels, biomass, alkaline electrolysis, polymer electrolyte, photo electrolysis and high temperature decomposition.
Energy requirement for electrolysis at 900 °C is less than what is required at lower temperatures like 150 °C. Therefore, overall electric efficiency is high for higher temperature compared to lower temperatures. A typical example of such high temperature technology is solid oxide electrolysis cells (SOECs) which have gained attention in the recent years [3]. SOEC is based on solid oxide fuel cells (SOFC) technology but operate in regenerative mode. SOEC uses a solid oxide electrolyte to produce hydrogen and oxygen. As the fuel cell technology is somewhat established, full cycle efficiency of SOEC can go up to 60%. SOEC consists of electrodes separated by an electrolyte. Single cells are rarely used for practical applications. Multiple cells are stacked in series for accumulated output. Interconnects, in between individual cells, are used to electrically connect multiple cells [4]

In a way of making SOEC operational on an industrial scale, it is very important to make cost effective components like electrolyte, electrodes and interconnects. It is of prime importance to overcome the challenges in order to make interconnects efficient in terms of performance and cost for commercialization of SOEC. Ferritic stainless steel is the widely used material for interconnects, though there are set of challenges which are discussed in later sections.

1.2 Aim of the Thesis

A major challenge is to produce SOEC in a cost effective way, which involves increase in the lifetime of the cells and reduction in the material cost. Anode side of SOEC experiences high pO_2 as it is exposed to oxygen, air containing atmospheres whereas cathode side is exposed to water vapor and hydrogen containing environments. Therefore pO_2 on cathode side is several magnitudes lower when compared to that of anode.

Interconnect materials are exposed to diluted environments due to safety regulations involved in usage of pure hydrogen gas. It is of scientific interest to find out how diluting the environment will affect the oxidation behaviour of interconnect materials in fuel environment. The research was aimed at studying the effect on oxidation behavior of steels when the amounts of hydrogen and water vapor are varied in the environment. The influence of varying amounts of water vapor and hydrogen content in a gas stream on the corrosion rate of AISI 441 ferritic stainless steel and Crofer 22 APU steel by keeping constant pO_2 was studied. Cathode/fuel side atmosphere of an operating SOEC was simulated in the laboratory and steels were tested.

To evaluate the performance of the material, ex-situ characterization techniques like scanning electron microscopy, energy dispersive X-Ray spectroscopy and gravimetric techniques were used. Additionally to access the electrical properties of the oxidized steel, area specific resistance was also measured in the case of Crofer 22APU steel.

1.3 Electrolysis Cells

An electrolysis cell is an instrument where the electrical energy is converted to chemical energy. Such cells consist of electrodes (anode and cathode) which are held apart and are maintained in contact with electrolyte (solid and liquid). These electrodes get charged when supplied with direct electric current (anode with positive and cathode with negative charge). Positive ions in the electrolyte are attracted to the cathode where reduction takes place (Eq. 1). On the other hand, negative ions migrate to the anode and get oxidized (Eq. 2) [5]. This can be applied to electrolysis of water as seen in Fig 1.

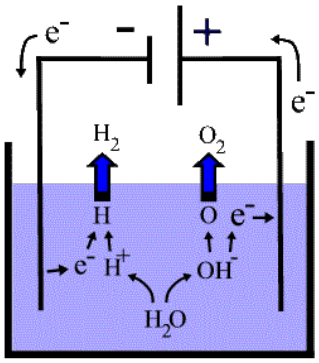

Fig 1: Schematic showing electrolysis of water [6]

Reactions in an electrolysis cell:

$$2\mathrm{H}^+ + 2e^- \rightarrow H_2 \quad (1)$$

$$4OH^- \rightarrow O_2 + 2H_2O \quad (2)$$

Overall reaction:

$$Energy\ (electricity) + 2H_2O \rightarrow O_2 + 2H_2 \quad (3)$$

Unlike spontaneous galvanic cells, an external power source is employed in this case to drive the reaction. Thus, a non-spontaneous reaction takes place in electrolytic cells. The difference between theoretical potential (calculated) and actual potential, which is called over potential, is needed to overcome the activation energy barriers for electron transfer at the anode and cathode interfaces [7]. The potential required to drive the reaction is derived from Nernst equation (Eq. 4).

$$\mathrm{E}_{cell} = \mathrm{E}°cell - \frac{RT}{nF}\ln(Q) \quad (4)$$

where E-cell potential, E°-cell potential at standard conditions, R-Universal gas constant, T-temperature, n-coefficient of transferred electrons, F-Faraday's constant, Q-reaction quotient of the reaction

1.4 Operating Principle of SOEC

The important components of an SOEC are ionic conducting electrolyte and the porous anode and cathode. Steam is fed at the cathode and an electrical potential is applied. Therefore, water molecule is electrolyzed, i.e., split into hydrogen and oxide ions at the electrode (Eq. 5) and the residual steam is separated. There is a gradient of water molecules along the length of the cathode. Oxygen ions travel to the anode (oxygen electrode) through the electrolyte. At the anode, these ions get oxidized i.e., they release electrons (Eq. 6) (Fig. 2) [8].

Cathode reaction: $$H_2O + 2e^- \rightarrow H_2 + O^{2-} \quad (5)$$

Anode reaction: $$O^{2-} \rightarrow \frac{1}{2}O_2 + 2e^- \quad (6)$$

Reactions:

Overall Reaction: $$Energy\ (electricity) + H_2O \rightarrow \frac{1}{2}O_2 + H_2 \quad (7)$$

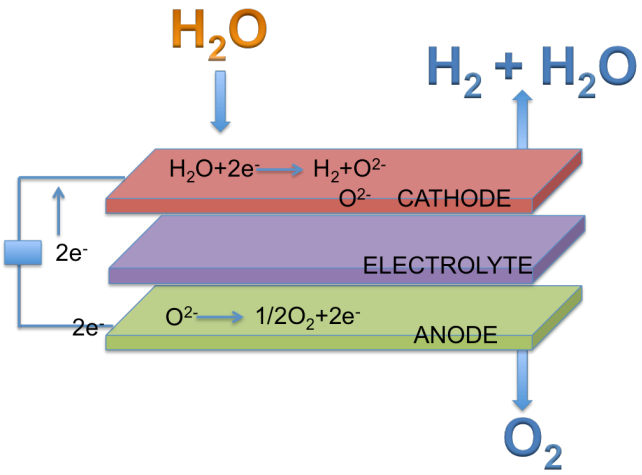

Fig. 2: Schematic showing SOEC functioning

The total energy required for hydrogen production in an SOEC is given by:

$$\Delta H = \Delta G + T\Delta S \quad (8)$$

where ΔG is the required electrical energy and TΔS is the thermal energy demand. From the above relation it can be inferred that the required electrical energy decreases with increased temperature which increases thermal energy. Thus, total energy requirement varies very little with temperature involved (Fig 3) [9].

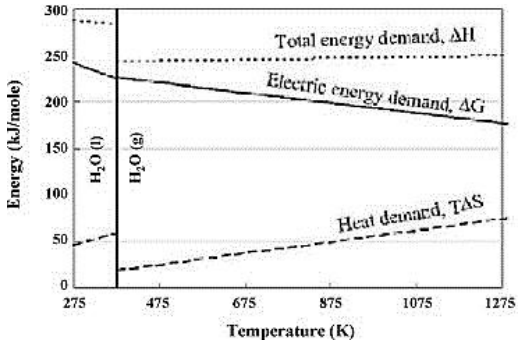

Fig 3: Thermodynamics of water electrolysis [9]

A typical SOEC consists of an electrolyte, mostly Y_2O_3 doped ZrO_2 sandwiched between electrodes. Materials used for electrodes are generally La-magnanite for cathode and Ni/ZrO_2 cermet as anode. Electrodes are deposited on sintered electrolyte along with interconnect (made from ceramics or high temperature stable material) to form a cell [10].

The voltage of the cell is given by free energy expression (Eq. 9) and is in the order of 1.1-1.2 V per cell, without taking overvoltage into account.

$$\Delta G = -nFE \quad (9)$$

As mentioned earlier, multiple cells are stacked in series and interconnects are used for electrical conduction. This stacking of cells varies according to the pattern of stacking, power density and geometry. The major classes of stack design are tubular design and planar design. Planar design is also known as flat plate design (Fig. 4). Modern day SOEC are of planar design as it can deliver cheaper units. Monolithic design development is underway [10].

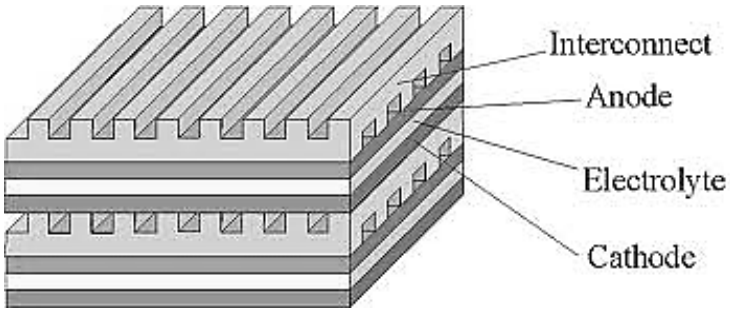

Fig. 4: Stack sequence in SOEC [11]

1.5 Cell Components

The four main cell components are anode, cathode, electrolyte and interconnect. The properties required for cell components are [4]:

1. Compatibility with other cell components in terms of chemistry and thermal expansion co-efficient (TEC).
2. Stability in the exposed environments.
3. Strength to withstand loads at service temperatures
4. Cost effective component fabrication

1.5.1 Electrolyte

The purpose of electrolyte is to conduct ions. It should not conduct electrons to avoid leakage current for higher efficiencies and be stable in the anode and cathode environments. Popular electrolyte material used is yttria stabilized zirconia (YSZ), but Scandia stabilised zirconia and gadolinium doped ceria are also used as electrolyte material. ZrO_2 based materials are considered to be best. Dopants for ZrO_2 are selected based on the structural differences they bring which facilitate oxygen conductivity. The structure of ZrO_2 is monoclinic up to 1170 °C, after which it changes to tetragonal and upon further heating to 2370 °C it changes to cubic. When doped with Y_2O_3, Zr^{+4} ions are replaced with Y^{3+} (slightly larger) ions. This replacement also affects O^{2-} ions by changing the number of O^{2-} ions as three O^{2-} ions replace four O^{2-} ions [12].

YSZ permits O^{2-} ions conduction and this conduction increases as the temperature increases. As the amount of Y_2O_3 increases, ionic conductivity increases and reaches saturation at 8% Y_2O_3, beyond which conductivity decreases.

1.5.2 Electrodes

Porous electrodes are adherent to dense electrolyte forming multi layered cell. This has to withstand different thermo mechanical loads. Since these components are brittle in nature, mechanical properties are also important which are addressed by proper cell design and optimized operating conditions.

1.5.2.1 Cathode

Cathode should be active to reduce steam and porous to allow the gas to flow out and to collect the fuel from the electrode. Porosity has to be maintained throughout its lifetime. Typical cathodes are made out of Ni-YSZ which, is 30% Ni added in the cermet to ensure the required TEC, electrical conductivity and good adhesion to the electrolyte. This remains as one of the best alternatives in the available cathode material options. New electrodes like $(LaSr)TiO_3$, SDN-Ni are under development. Metals like Ni, Co, Ru and Pt can be used but Ni is used for economic reasons [13].

1.5.2.2 Anode

The requirements for a good anode are electronic and ionic conductivity along with porosity. It should withstand oxidizing environments and it is desirable that the morphology remains unaltered during the service life of the cell. A mixture of lanthanum strontium maganite (LSM) is a popular material used as an anode. Recent research reports the use of (porous perovskite structure) lanthanum strontium cobalt ferrite (LSCF) to replace LSM. $LaMnO_3$ is doped with Sr to increase the electronic conductivity and also TEC [14].

1.5.3 Interconnector

As mentioned earlier, electrolysis cells are stacked in series for the required output. The interconnect is the component which, physically separates but electrically connects the cells. Electrical connection means connecting anode of one cell to cathode of the neighboring cell. It also helps in separating individual cells to avoid mixing of gases (hydrogen & oxygen) or gas leakage between the cells. They also have role in supporting the stack structure mechanically. Being in contact with both the electrodes calls for the stability of the interconnect material in both the electrode environments.

As interconnectors serve the above mentioned roles, the material requirements for this purpose are highly demanding among the four components. Commercial viability of SOEC depends largely on interconnect material development.

Below are a few characteristics required for an interconnect [15]:

- It should be electrically conductive in the cell atmosphere (both anode and cathode).
- It should possess stability in terms of microstructure, chemical composition, creep resistance, mechanical strength and dimensional stability in the intended conditions of temperature and atmosphere. Any degradation in the above mentioned properties will lead to a low stack performance.
- It should have very low permeability to avoid mixing gases from anode and cathode. TEC should match well with that of electrodes and electrolyte to avoid thermal stresses [15]. No reaction should be expected between interconnect and its adjacent electrode material.
- The important of all is its oxidation resistance. It is a prerequisite for interconnect material to possess resistance to oxidation and carburization. Reasonable thermal conductivity is expected from interconnectors [16].
- Last of all is the ease of fabrication. It should also be economical to fabricate on large scale [17].

Demanding technical requirements of interconnect material pose challenge for viable systems commercially.

1.5.3.1 Ceramic Interconnectors

There are very few oxides which fulfil the stringent requirements to be a candidate material for interconnectors. One among them is lanthanum chromite ($LaCrO_3$). It has good electrical conductivity combined with reasonable chemical stability in the operating conditions. It also has fairly good compatibility with electrodes in terms of chemistry and TEC. To improve the existing properties, $LaCrO_3$ is doped with Co, Ni, Fe, Mg, Cu, Sr. But this doping adversely affects few of the required properties. Ceramic interconnects involve high cost of production. It is also prone to warping, when there is partial reaction between H_2 and interconnect, which will adversely affect the performance of stack [16].

1.5.3.2 Metallic Interconnectors

Metallic materials are better in terms of electrical and heat conductivity compared to ceramics. Electrical conductivity of metals is several orders higher compared to ceramics. Ohmic losses are very small and can be neglected. Additionally, they involve low cost and easy fabrication. These advantages make metallic materials more suitable for interconnectors compared to ceramics. The limitation with regard to metallic materials is the degradation of stack performance at high temperatures. This is due to the development of a semi-insulating oxide layer over time during operating conditions [18]. This layer increases the contact resistance between the interconnect and its neighboring components. If there is an increase in the resistance, electrical efficiency of the stack decreases even though the efficiency of individual cells is high. For a commercial metallic interconnect, electrical resistance over interconnect should be a minimum for high stack efficiency.

Development of the oxide scale on metallic interconnect is inevitable in the oxidizing environment at high temperatures. So manipulation of oxide scale to minimize the contact resistance becomes important. It is important that the oxide growth is very slow for the projected lifetime in both cathode and anode atmospheres

in order to exhibit satisfactory electrical conductivity at operating conditions. The oxide scale should adhere to the metal substrate and withstand thermal cycling but not spall off or delaminate. TEC of the metal substrate and the oxide formed should be similar to avoid stresses [4].

Noble metals cannot be used due to their limited availability and high costs involved which leaves high temperature alloys as possible candidate materials. Alloys which form alumina scales cannot be used due to lower electrical conductivity values of the scale though the scale exhibits very good high temperature properties. Silica forming alloys are also ruled out due to the embrittlement caused by large amounts of silicon and also due to the electrically insulating nature of the scale.

Table 1: Electrical Resistivity of Oxides in Air at 800 °C (approximate) [19]

Oxide	Resistivity (Ω *cm^2)
SiO_2	10^6
Al_2O_3	10^8
Cr_2O_3	10^2

Ni based superalloys have high TEC and form an alumina scale. Thus, iron based chromia forming alloys are the best suited for interconnectors. Chromia has better electrical conductivity compared to Al_2O_3 and SiO_2. However, the drawback with pure Cr_2O_3 forming alloys is the formation of volatile gaseous Cr species in the oxygen side of cell which poisons the oxygen electrode at operating conditions [20].

Evaporation of chromium also leads to depletion of the same in the substrate alloy. If the Cr content is too low the diffusion is too slow to form a protective chromia layer and a crack or defect will result in a very rapid break away corrosion resulting in mechanical failure. As it is known that stainless steels form chromia as protective scale, austenitic and ferritic steels are the options left. Between the two, ferritic stainless steel has matching TEC with the other components of the cell compared to that of austenitic stainless steels. Ferritic stainless steels are also resistant to carbon dusting unlike austenitic stainless steels [20].

Therefore, Fe-based ferritic stainless steel interconnects are used which contain around 18-23 wt% Cr. These alloys are relatively stable at operating temperatures of SOECs. These alloys possess high formability and machinability. Manganese in the alloy typically causes a formation of Cr_2MnO_4 spinel on top of Cr_2O_3. Therefore, the chromium volatilization can be decreased with this group of alloys since the spinel acts as a cap layer [21]. Coating of interconnect with oxides can increase the performance as they reduce the oxidation rate of substrate. Examples of ferritic stainless steels used for interconnect are Crofer 22APU, Crofer 22H, Sandvik Sanergy HT with optimized properties [22].

1.6 Corrosion

Corrosion may be defined as material destruction or deterioration due to reaction with its environment. Corrosion can be classified in different ways. One major classification is atmospheric corrosion, aqueous corrosion and high temperature corrosion. One method of division is low temperature and high temperature. Another is wet corrosion and dry corrosion. Corrosion can also be defined as reverse extractive metallurgy. The main interest in the present study is about high temperature corrosion [23].

High temperature corrosion can be defined as chemical attack on material from gases or salts typically at temperatures above 400 °C. Carburization, oxidation, sulphidation are few typical examples of high temperature corrosion. It should be noted that material selection for high temperature application does not only depend on corrosion resistance but also on mechanical and creep strength of the material.

Almost all metals, alloys and materials of our interest for different technological application will oxidize or corrode at high temperatures. Thermodynamics and kinetics of the corrosion depends on the environment and temperature. Most of the metals and alloys exposed to high temperature oxidize which leads to change in physical properties. High temperature corrosion is not limited to only gaseous attack but also solid or molten salts. High temperature corrosion is also known as dry corrosion or scaling [23].

1.6.1 High Temperature Corrosion

Most of the metals in their working conditions are exposed to atmospheres in which they form oxides, sulphides or carbides depending on the ambient gases present. This kind of reaction is less prevalent when the temperature is low or at room, as the kinetics are low [24].

As the rate of reactions increase with increase in temperature, corrosion resistance becomes of paramount importance. High temperature corrosion is one of the main problems for materials being used at elevated temperatures. Material deterioration leads to reduction in load bearing area.

$$aM + \frac{b}{2}O_2 \rightarrow M_aO_b \tag{10}$$

The above is total chemical reaction of a metal M and O_2 to form oxide. This reaction might look simple, but the path followed by reaction, oxidation behavior of metal and many other factors can make an oxidation reaction complex. At higher temperatures, there is increase in reaction rate, which is increase in kinetics.

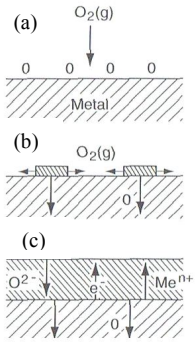

Figure 5: Schematic of oxidation on a metal surface (a) adsorption of oxygen gas, (b) oxide nucleation and lateral growth and (c) increase in thickness of the oxide layer by ion diffusion [24]

Oxide formation can be explained in 3 steps:

a) Adsorption of oxygen on the metal surface
b) Reaction of metal and oxygen which results in oxide nucleation and growth until a continuous film is formed
c) Growth of the oxide film in the perpendicular direction to the metal surface

The above illustration shows step wise process of oxide formation on a metal substrate (Fig. 5). In the first step, oxygen is adsorbed on the metal surface. After which oxygen dissolves with the metal and nucleation of oxide occurs. After nucleation, oxide layer is grown in lateral direction and a continuous film is formed. It should be noted that initial adsorption and oxide nucleation depends on surface orientation, crystal structure at the surface, surface roughness and impurities in the metal and gas. This oxide layer isolates the metal surface from gas. If the film is continuous in nature, then the reaction will no longer follow the first step. Solid state diffusion of the reactants through the film governs the reaction to proceed. At this stage the oxide film grows in the direction perpendicular to metal surface through solid state diffusion.

1.6.2 Thermodynamics of Metal-Oxygen reactions

The second law of thermodynamics tells whether a reaction is possible or not. It is written in terms of free energy, enthalpy and entropy at constant pressure associated with the reaction Eq. 11 [25].

$$\Delta G = \Delta H - T\Delta S \tag{11}$$

If $\Delta G>0$, then the reaction is non-spontaneous and if $\Delta G=0$, reaction is in equilibrium. If $\Delta G<0$, then the reaction is spontaneous in nature.

The driving force for metal-oxygen reaction is the free energy change associated with the oxide formation. It is expressed as

$$\Delta G = \Delta G^O + RT \ln \frac{a(M_aO_b)}{a(M)^a a(O_2)^{\frac{b}{2}}} \tag{12}$$

Where $\Delta G°$ is the free energy change at standard conditions, R is universal gas constant, T is the temperature, a is the thermodynamic activity of the species. The activity of metal and metal oxide can be assumed to be unity.

Therefore Eq. 12 changes to Eq. 13 when the unit value of activity is substituted

$$\Delta G = \Delta G^O + RT \ln \frac{1}{(O_2)^{\frac{b}{2}}} \tag{13}$$

When the Eq. 13 is in equilibrium then, ΔG = 0 and thus

$$\Delta G^{O} = -RT \ln \frac{1}{(O_2)^{\frac{b}{2}}} \tag{14}$$

The activity of O_2 is partial pressure of oxygen, thus Eq. 14 changes to

$$pO_2 = -\frac{\Delta G^{O}}{RT}\frac{2}{b} \tag{15}$$

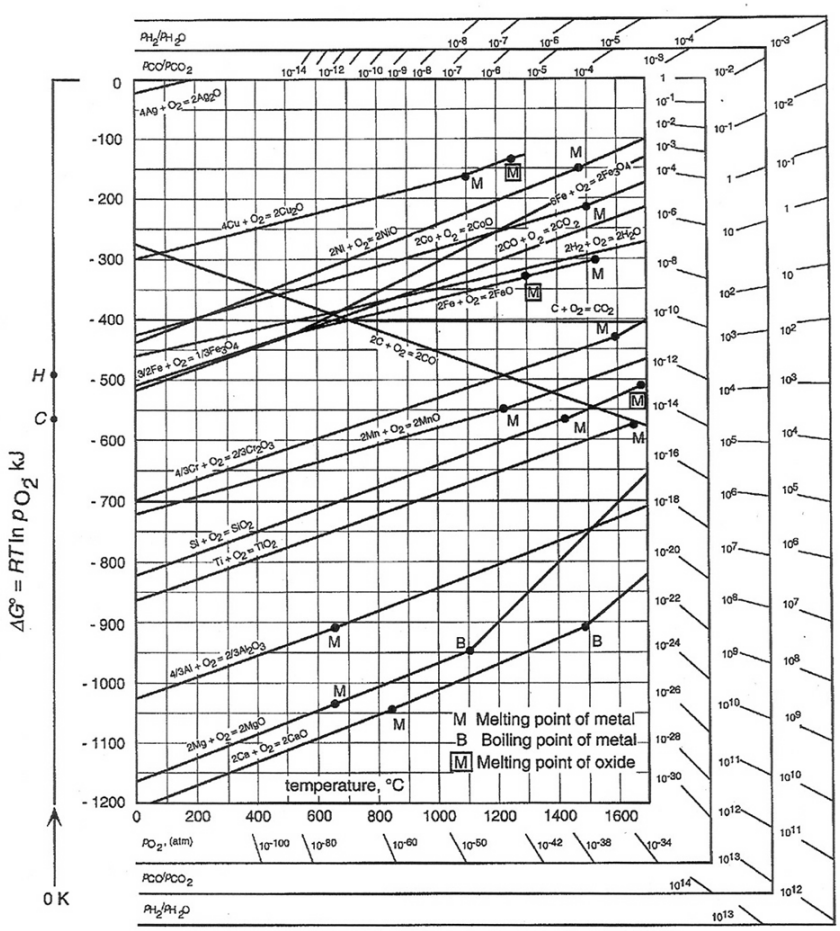

Figure 6: Ellingham/Richardson diagram for various metals [26]

The partial pressure of oxygen is called dissociation pressure when formation of oxide is in equilibrium with dissociation of oxide. If the pressure is less than the dissociation pressure, oxide is reduced to metal and metal is oxidized if the pressure is more. The standard free energies of formation of oxides as a function of temperature and the corresponding dissociation pressures of the oxides are summarized in the form of Ellingham/Richardson diagrams (Fig. 6). The slopes in the diagram are positive since the standard entropies of formation of metal oxides are negative. The most stable oxide has largest negative values of free energy change. The lower the line in the diagram, the more stable is the oxide compared to the ones above it. This diagram helps in knowing the stability of oxide for metals and the type oxide that can form on alloys.

1.6.3 Kinetics

Though thermodynamics gives an idea about feasibility of oxide formation, it does not give any information about the rate of reaction. Corrosion rate is important to predict the life time of the material and is often measured in terms of weight change of the sample over an extended period under given conditions.

Rate of reaction and their equations of metal oxidation can depend on temperature, oxygen partial pressure, elapsed time of reaction, surface condition and crystallography. These rate equations are not sufficient to interpret oxidation mechanisms but help in classifying them. Rate determining steps generally are electrons or

ions transportation due to electric fields in or across the oxide film. Rate equations can be classified as logarithmic, parabolic and linear (Fig. 7). Deviations from these rate equations are also seen. It is difficult to fit rate data to simple rate equations since many mechanism can be in play at the same time [24].

1.6.3.1 Logarithmic Rate Equations

Logarithmic rate is seen in large number of metals at temperatures below 400 °C. Characteristic of this kind of rate equation is reaction rate is quite rapid in initial stages and then drops to negligible rates. Logarithmic behavior includes direct logarithmic and inverse logarithmic rate equations (Eq. 16 and Eq. 17).

Direct logarithmic reaction: $$x = k_{log} \log(t + t_0) + A \quad (16)$$

Inverse logarithmic reaction: $$\frac{1}{x} = B - k_{il} \log t \quad (17)$$

x represents the thickness of the oxide film, amount of oxygen consumed by the metal for oxidation per unit surface area, and amount of metal consumed for oxide transformation, t is the exposure time. k_{log} and k_{il} are the rate constants and A & B are constants. A number of theories based on rate determining step have been put forward for logarithmic rate equations [24].

1.6.3.2 Parabolic Rate Equation

Parabolic equation can be fit when the rate controlling step for oxidation is ionic diffusion through oxide scale. As growth rate is only dependent on the diffusion of ions or electrons through the oxide scale, the rate will decrease with time due to the increasing length of the diffusion paths as the oxide scale thickens. The oxide thickness increases in parabolic nature with time. The oxide grows in parabolic fashion with respect to time and is expressed as below.

$$x^2 = k_p\, t + C \quad (18)$$

where x represents the oxide thickness, k_p is the parabolic rate constant, t is the time and C is the integration constant. This is generally seen in many metals which oxidize at high temperatures. This kind of behavior is desirable as this is characteristic of protective oxide scales [24].

1.6.3.3 Linear Rate Equation

Unlike parabolic and logarithmic rate equations where reaction rate decreases with increasing time, linear rate oxidation is constant with time. Therefore, it is independent of the amount of gas or metal consumed. Linear oxidation may be described by

$$x = k_1\, t + C \quad (19)$$

where k_1 is the linear rate constant, t is the time and C is the integration constant. As the reaction is linear, surface or phase boundary reaction will be rate determining step. Oxide scale of this nature is very thin and non-protective.Linear oxidation is also observed if the oxide film is destroyed by e.g. spalling off and which is referred to as break away corrosion. In detail, breakaway corrosion is the combination of two rate mechanisms. Initially, parabolic behaviour is observed which is followed by linear behaviour. Protective oxide scale breaks after some time giving way to linear behaviour which is not protective. This can be seen when the protective species in the alloy is all used up or depleted [24].

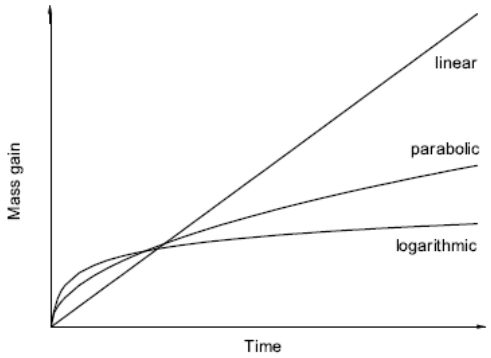

Figure 7: Mass gain curves for growth mechanisms [27]

1.7 Challenges Related To Interconnects:

Chromia forming alloys are the best candidates for interconnectors owing to their high temperature oxidation resistance. Interconnects are exposed to moist hydrogen on one side (cathode side) and oxygen on the other side (anode side). Due to the high temperatures involved and the presence of moisture in the atmosphere, corrosion is the major challenge encountered in interconnects. Corrosion not only degrades the mechanical performance of interconnect due to chromium evaporation but also adversely affects the electrical conductivity. Reactive elements such as Zr, Ce, La etc., are added in small quantities to improve the corrosion resistance of chromia and alumina forming alloys. It has been reported that thin coatings of reactive elements not only improved corrosion resistance but improved the oxide scale adhesion of chromia forming alloys [28].

The following section discusses the problems related to electrical conductivity and chromium evaporation of interconnects.

1.7.1 Electrical Conductivity

The ability to conduct electric current of interconnectors is usually quantified in terms of area specific resistance (ASR, Ω/cm^2) which increases as the oxide layer thickness grows thicker. It is established that resistance increases which increase in thickness of oxide scale [29]. The contact resistance of metallic interconnect is responsible for the drop in electrical efficiency and premature failure of the stack over the projected service lifetime.

It should be noted that there are two effects on the magnitude of scale resistance due to increase in temperature. One is increase in the resistance due to scale thickening as temperature increases. The second effect is that since the oxide scale is a semiconductor, which means its conductivity increases with increase in temperature resulting in decrease in resistance. Coatings employed for oxidation resistance should also possess low electrical resistance. These coatings can also change the conduction mechanisms in oxide scales by changing the required activation energy. Activation energy required for conduction in oxide scale is different when an uncoated alloy is compared to that of a coated alloy sample [30].

Oxide scale is developed on both sides of metallic interconnect under SOEC operating conditions. Therefore, ASR is the sum of resistance of oxide scale and metal substrate together. But the resistance of the substrate can be comfortably neglected for its very low value as compared to oxide scale resistance value. Presence of cracks at the metal/oxide interface increases the resistance.

The conductivity of a material changes with temperature as:

$$\sigma = \sigma_o \, e^{\frac{-E_a}{kT}} \tag{20}$$

where E_a is the activation energy, k is the boltzmann constant and T is the temperature. Electrical resistance activation energy is a barrier for conduction. Increase in activation energy is mainly due to oxide layer growth. Slope of ln (conductivity) Vs. (1/T) plot gives activation energy for conduction [31]. Activation energy is lowered with increasing manganese content in the chromium manganese spinel. This makes them suitable for the interconnect. To decrease the electrical resistance of interconnect, it is essential to improve the oxidation resistance by modifying the composition without altering the mechanical and physical properties or usage of coatings on the existing alloys [32].

1.7.2 Chromium Evaporation

Mixture of water vapor and oxygen is more detrimental for the corrosion resistance of ferritic stainless steels compared to dry oxygen. Under thermodynamically unstable conditions, a chromia scale in the presence of humid air forms CrO_3, $CrO(OH)_2$ and $CrO_2(OH)_2$. These species are volatile in nature and lead to chromium evaporation [33]. If the amount of Cr decreases below the critical value required for the formation of protective scale due to corrosion, it leads to breakaway corrosion.

The following are the reactions leading to chromium evaporation.

$$\frac{1}{2}Cr_2O_3 + \frac{3}{4}O_2 \rightarrow Cr_2O_3(g) \tag{21}$$

$$\frac{1}{2}Cr_2O_3 + H_2O + \frac{3}{4}O_2 \rightarrow CrO_2(OH)_2 \tag{22}$$

The influence of gas velocity should also be considered in this context as there is increase in the velocity the nature of oxide changes from protective to that of non-protective one. This has been explained by Asteman et al since the volatile species are carried away by the gas stream after they diffuse from the stagnant layer of gas close to surface metal surface [34]. As the flow rate increases, evaporation rate also increases [21].

To counter chromium evaporation, coatings can be used. Much research has gone into the field of coatings for interconnect to counter chromium evaporation. Coating techniques like metal-organic chemical vapour deposition (MOCVD), large area filtered area deposition and hybrid filtered arc assisted electron beam physical vapour deposition are used [35]. Different coatings have been tried of which spinel coatings are important. Spinel coatings have gained much attention since they generally adhere to the substrate and also have good electrical conductivity [36].

2 EXPERIMENTAL TECHNIQUES AND MATERIALS

2.1 Materials and Preparation

Materials under investigation are uncoated AISI 441 and CROFER 22 APU steels. Composition of the alloys is given in Table 2. The investigated materials were received in the form of sheets of 0.3 mm thickness. These sheets were cut into 1.5 X 1.5 cm^2 specimens using cutting machine. The specimens obtained after cutting were cleaned in acetone and then ethanol, using an ultrasonic bath. Then the samples were weighed using Mettler Toledo XP6 balance.

Table 2: Composition of the materials used:

Steel	Cr	Mn	Ti	Nb	Si	Ni	C	N	S	P	Al	La
AISI 441	17.56	0.35	0.173	0.39	0.59	0.26	0.014	0.017	0.001	0.03	-	-
CROFER 22 APU	22.2	0.46	0.06	-	0.03	0.02	0.005		0.02	0.016	0.02	0.06

2.2 Experimental setup

The samples have been exposed to 850°C in a tube furnace to different atmospheres. The specimens were placed parallel to each other in an alumina holder. Each holder holds up to 6 samples and 5 such holders were used for one run of the furnace. The total gas flow rate was fixed at 250 ml/min for all the experiments. Samples were placed parallel to the gas flow. As the simulated atmosphere was that of the cathode side of SOEC, moist Ar-H_2 gas was used for the exposures. Equipment surrounding the furnace was constructed to facilitate the introduction of water vapor into Ar-H_2 gas. Ar-5%H_2 gas was bubbled through water, which was kept at 82 °C, and the required level of humidity was adjusted and monitored using a thermostat. Before the start of experiment, humidity was monitored with a chilled mirror sensor (Optidew Vision). The H_2/H_2O ratio which is pO_2 was kept constant throughout the experiments. Pure Ar gas was used for different levels of diluting hydrogen and water vapor in the atmosphere, without altering the H_2/H_2O ratio (pO_2 ~10^{-15} atm).

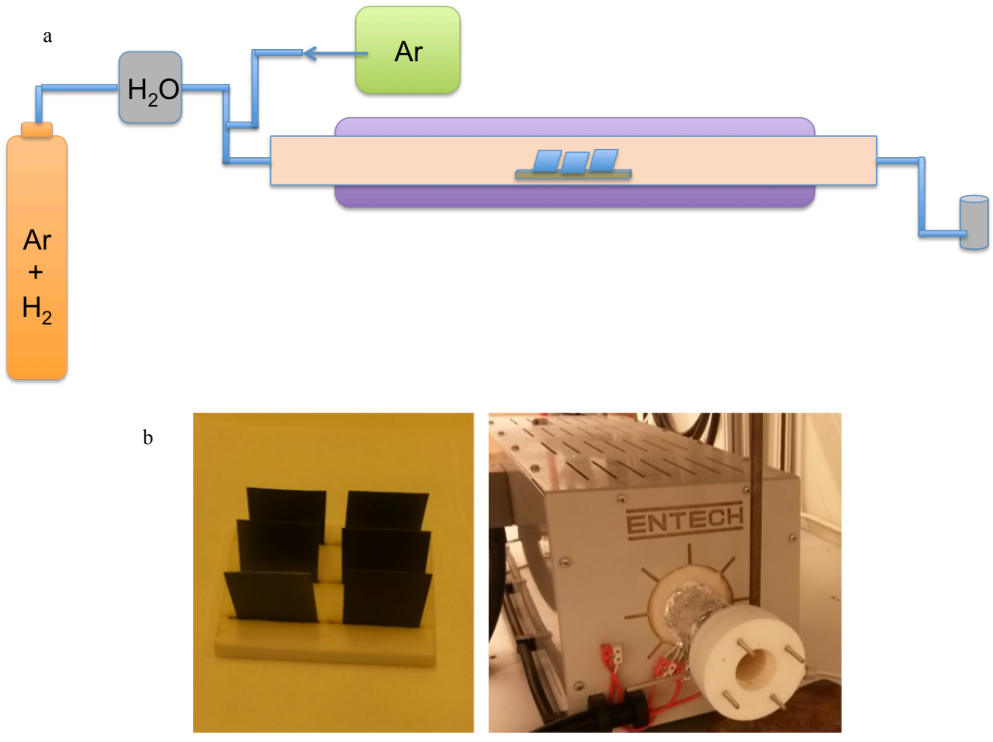

Fig 8: (a) Schematic of experimental setup, (b) Alumina holder with samples (left), furnace used for exposure (right)

The following is the matrix used for carrying out experiments.

Sample	Water content atmosphere	Atmosphere employed	Exposure (Number of hours exposed)
AISI 441C	40%	250 ml/min of 5% H2-Ar with 40% H20	24, 72, 168, 500
	20%	125 ml/min of 5% H2-Ar with 40% H20 125 ml/min of pure Ar gas	24, 72, 168, 500
	10%	75 ml/min of 5% H2-Ar with 40% H20 175 ml/min of pure Ar gas	24, 72, 168, 500
Crofer 22APU	40%	250 ml/min of 5% H2-Ar with 40% H20	24, 72, 168, 500
	20%	125 ml/min of 5% H2-Ar with 40% H20 125 ml/min of pure Ar gas	24, 72, 168, 500
	10%	75 ml/min of 5% H2-Ar with 40% H20 175 ml/min of pure Ar gas	24, 72, 168, 500

Exposures were carried in discontinuous fashion, which means that the furnace was cooled down to room temperature before each gravimetric measurement and placed back in furnace to continue the experiment. Heating rate of 2.5 °C/min was employed whereas cooling rate was low compared to heating. The specimens after being exposed were subjected to gravimetric analysis using Mettler Toledo XP6 balance. Difference in mass gain between before and after exposure was calculated. Samples were removed after 24 h, 72 h, 168 h and 500 h. All the samples in the furnace were weighed whenever the samples were removed from the furnace.

After the exposures, selected samples were subjected to characterization for better understanding of the mechanisms involved. Optical microscopy, Scanning electron microscopy (SEM) and energy dispersive X-Ray spectroscopy (EDS) were used. Few representative samples of Crofer 22 APU steel were subjected for electrical characterization.

2.3 Characterization Techniques

2.3.1 Optical Microscopy (OM)

The fundamental approach in OM is to prepare the sample for imaging by successive grinding and polishing of a surface until mirror finish and observe under the microscope. Oxidized samples cross-section were mounted and prepared for OM.

It should be noted that the resolution of microscope (shortest distance where two points can be seen separated distinctly) is around micrometer (10^{-6} m). If we compare with the resolution of the naked eye of 0.1 mm, this means a practical range of magnification of approximately 25-500 times. But other techniques such as SEM can be used to have an even higher magnification, and thus be able to focus on detail on what we are looking for [37].

2.3.2 Scanning Electron Microscopy (SEM)

In SEM, the sample is scanned by a focused beam of electrons, which will react with the atoms of the sample. It will produce different kind of signals, containing information on the surface of the sample, such as: local texture, grain boundary character, phase distribution, chemical contrast, topography, etc. SEM micrographs have a large depth field, thanks to the beam of electrons and the resulting image has a 3D appearance, useful for the understanding of the surface of the sample. Moreover the range of magnification is between 10 and 500,000 times. This type of microscope have a resolution around 5 nanometer (10^{-9} m) [37].

Cross-section and surface of the oxidized samples were studied using different modes (back scattered, secondary electrons and X-Rays) of analysis in SEM.

2.3.3 Electrical Characterization

ASR measurement involves the preparation of a contacting electrode with a defined surface area. Two different techniques were experimented for the electrode preparation in this study. The first technique involved electroplating a 1.0 X 1.0 cm^2 electrode using Ni bath (Fig 9(a)). The second technique involved painting ofa 1.0 X 1.0 cm^2 electrode using Ni paste and firing at 850 °C (Fig 9(b)). The second technique proved to be more effective of the two. Painting of the specimen was carried out in two steps. The first step was to apply a thin coat of Ni and fire. As a second step, a thick coat was applied and fired on the already painted and fired specimen. The prepared electrodes were characterized using a Probostat (NorECs, Norway) test cell connected to an impedance analyzer (Solartron 1260A). After that, it was placed in a tubular furnace. Each sample was characterized in the temperature range of 850 °C-500 °C for activation energy calculations. Electrical resistance was recorded and used for further calculations.

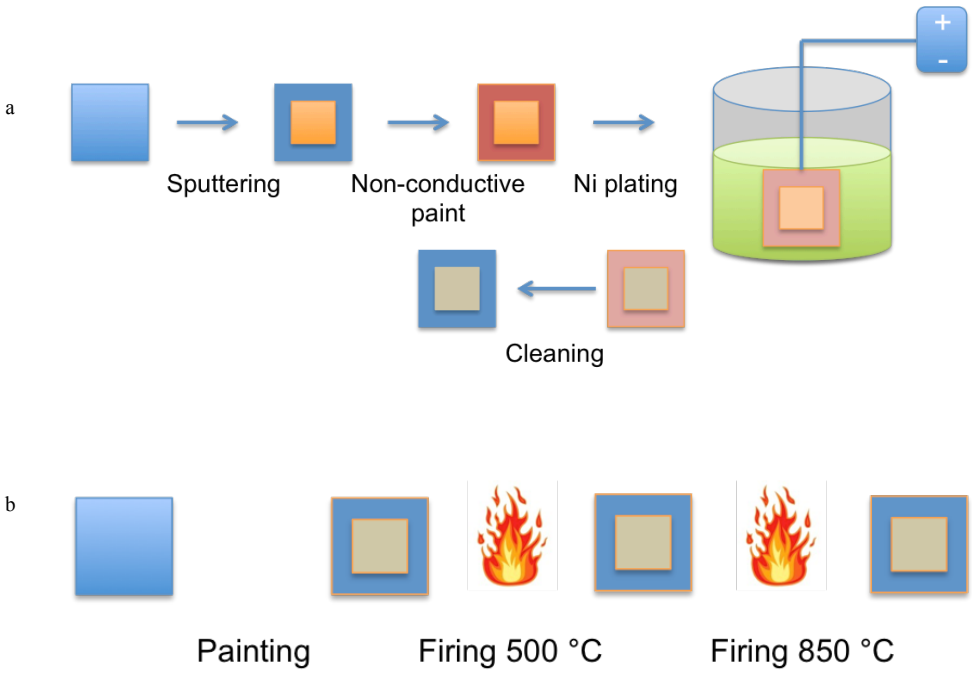

Figure 9: Electrode preparation for ASR measurement, (a) method 1 and (b) method 2

3 RESULTS

3.1 Gravimetric Analysis

Discontinuous method was employed to measure the mass gain of the exposed samples after 24 h, 72 h, 168 h and 500 h. The average mass gain obtained was plotted against the number of hours exposed. In general, the oxide scale growth rate of 441 steel was high compared to that of Crofer 22 steel as was evident from the average mass gain observations. No spallation was observed for any of the steels

3.1.1 AISI 441 steel

Mass gain was observed to be the highest for 441steel exposed for 500 h in Ar-3%H_2-40%H_2O atmosphere at 850 °C. It had the highest oxide scale growth rate with an average mass gain of 0.75 mg/cm^2 after 500h. As the water vapor content was diluted from 40% (Ar-3%H_2-40%H_2O) to 20% (Ar-1.5%H_2-20%H_2O), the oxide growth rate decreased from 0.75 mg/cm^2 to 0.50 mg/cm^2.

As the water vapor content was diluted further by a factor of 2, i.e., decreased from 20% to 10% (Ar-0.75%H_2-10%H_2O), no substantial decrease was observed in oxide scale growth (0.5 mg/cm^2 to 0.48 mg/cm^2) (Fig. 10). The extent of decrease in the rate was high when the water vapor content was diluted from 40% to 20% using Ar compared to the rate decrease from 20% to 10%.

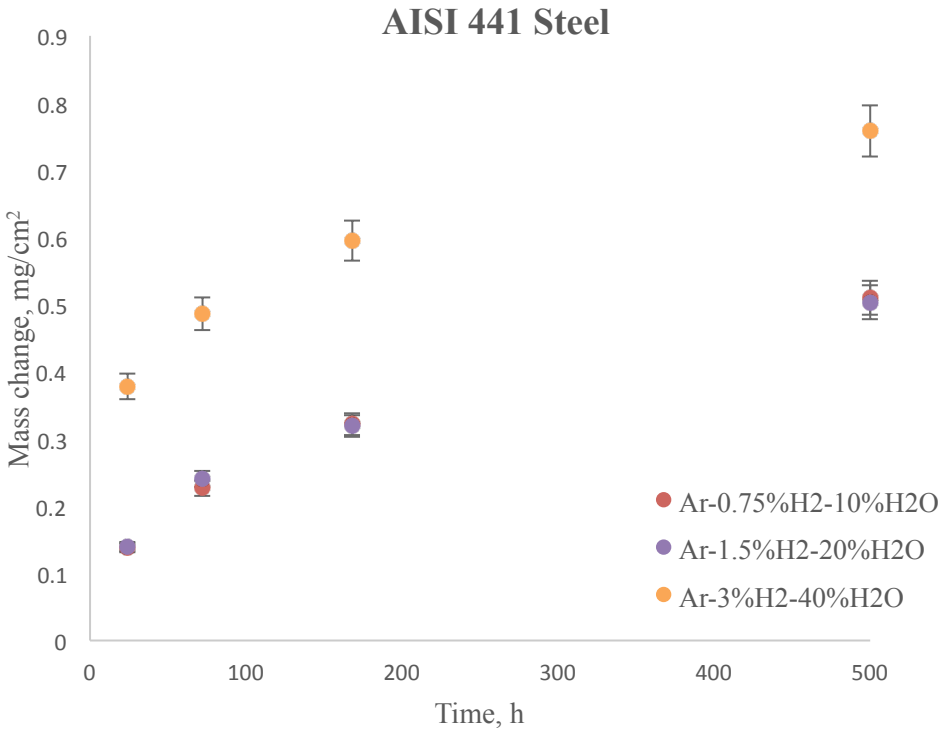

Figure 10: Mass gain of 441 steel in Ar-3%H_2-40%H_2O, Ar-1.5%H_2-20%H_2O and Ar-0.75%H_2-10%H_2O atmospheres

3.1.2 Crofer 22 APU

Mass gain observed in Crofer 22 APU steel when exposed for 24, 72, 168 & 500 h at 850 °C remained similar in all the Ar-3%H_2-40%H_2O, Ar-1.5%H_2-20%H_2O and Ar-0.75%H_2-10%H_2O environments. An average mass gain of 0.47 mg/cm^2 was observed after 500h in Ar-3%H_2-40%H_2O environment whereas for Ar-1.5%H_2-20%H_2O it was 0.47 mg/cm^2 and 0.46 mg/cm^2 for Ar-0.75%H_2-10%H_2O (Fig. 11).

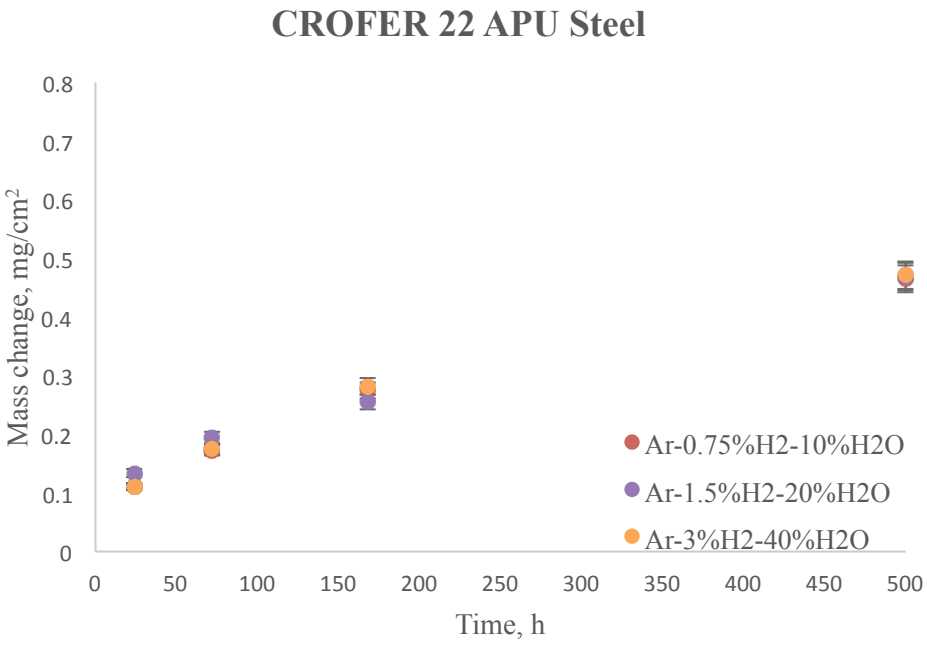

Figure 11: Mass gain of Crofer 22 steel in Ar-3%H_2-40%H_2O, Ar-1.5%H_2-20%H_2O and Ar-0.75%H_2-10%H_2O atmospheres

3.1.3 Mass gain square Vs. Time plots

k_p was calculated using mass gain per area square in place of oxide thickness of Wagner theory.
Wagner theory:

$$X^2 = k_p^* t \tag{23}$$

Where X is the scale thickness, k_p^* is the parabolic oxide rate constant and t is time for the scale to grow [24]. X replaced with Δm/A gives

$$\left(\frac{\Delta m}{A}\right)^2 = k_p t \tag{24}$$

As seen from linear fit plots of mass gain square vs. time (h), oxidation behavior for 441 steel was following parabolic behavior in Ar-1.5%H_2-20%H_2O and Ar-0.75%H_2-10%H_2O environments. Oxidation rate was deviating from the parabolic behavior in Ar-3%H_2-40%H_2O environment (Fig. 12). This is in line with the average weight gain value of the specimens in the respective environments. For Crofer 22 APU steel, the oxidation behavior of the specimen remained same in the three environments, k_p remains same (Fig. 13).

Table 3: Calculated k_p values

Environment	AISI 441 steel	CROFER 22 steel
Ar-0.75%H_2-10%H_2O	0.0005	0.0004
Ar-1.5%H_2-20%H_2O	0.0006	0.0004
Ar-3%H_2-40%H_2O	NA	0.0004

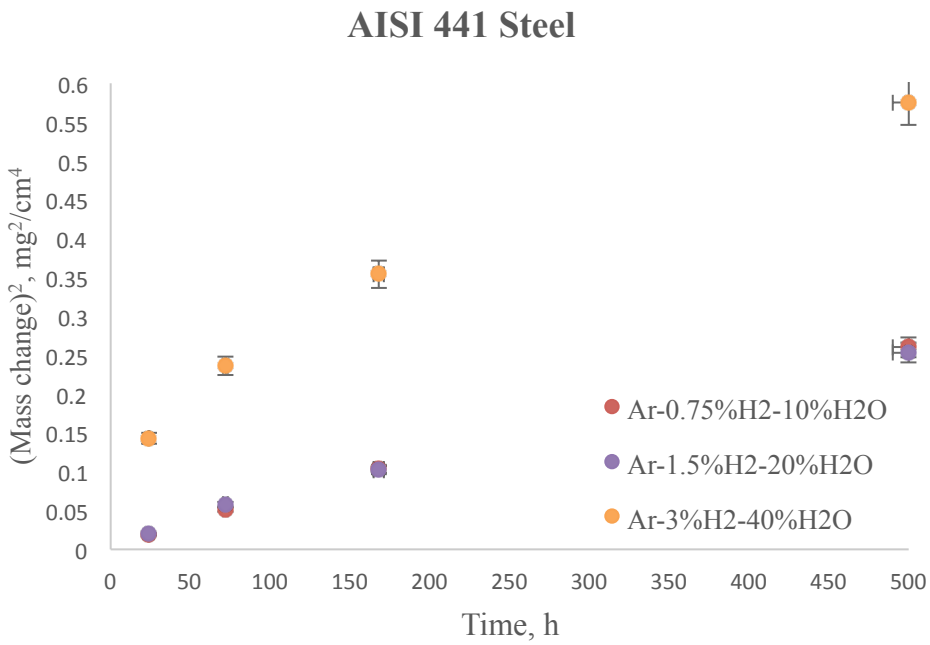

Figure 12: Mass gain square vs. time plots of 441 steel in Ar-3%H_2-40%H_2O, Ar-1.5%H_2-20%H_2O and Ar-0.75%H_2-10%H_2O atmospheres

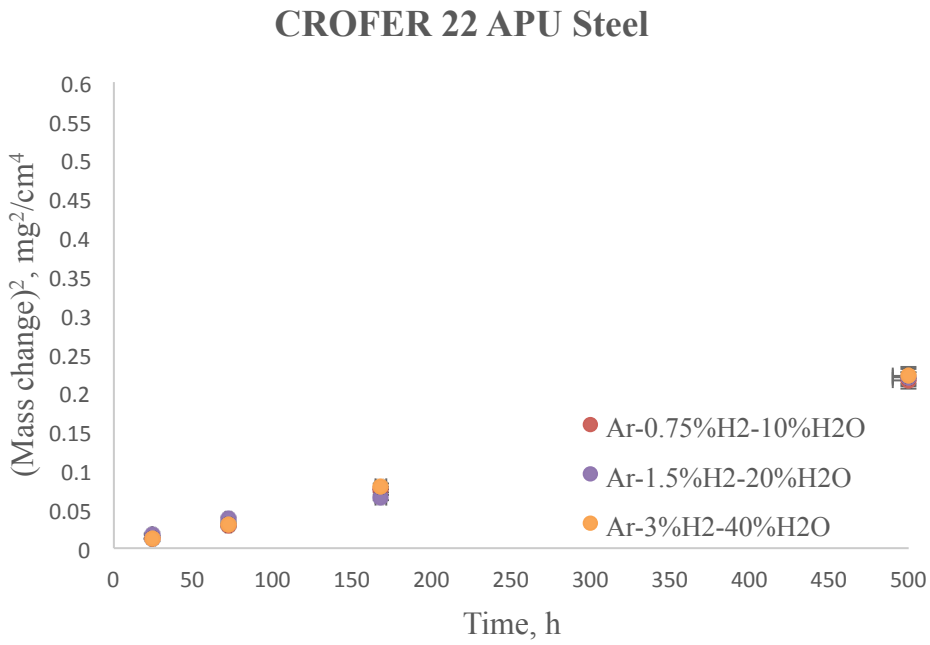

Figure 13: Mass gain square vs. time plots of Crofer 22 APU steel in Ar-3%H_2-40%H_2O, Ar-1.5%H_2-20%H_2O and Ar-0.75%H_2-10%H_2O atmospheres

3.2 Microstructure Evaluation

SEM evaluation was carried out on the specimens exposed to Ar-3%H_2-40%H_2O and Ar-0.75%H_2-10%H_2O environments assuming that Ar-1.5%H_2-20%H_2O environment specimen would have features

which fall in between the former two. In the same way specimens exposed for 24 hours and 500 hours were analyzed for simplicity in understanding the oxidation behavior. It should be noted that individual oxide layers were difficult to resolve in the oxide scale.

For ease of understanding, 441 steel was considered first

3.2.1 AISI 441 Steel

3.2.1.1 Ar-3%H_2-40%H_2O environment

SEM analysis of the cross section of steel exposed for 24 h at 850 °C revealed a uniform dense oxide scale (Fig. 14). Internal oxidation at alloy/scale interface was seen at a few locations. The porosity in the scale was negligible and the scale was more or less uniform in thickness. The oxide scale was very thin and the thickness was approximately around 1.5 μm.

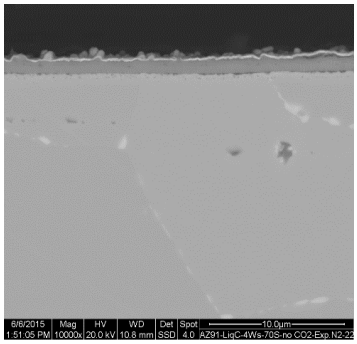

Fig 14: SEM photomicrographs showing the cross section of 441 steel exposed for 24 h at 850 °C in Ar-3%H_2-40%H_2O environment

Based on EDS analysis, the scale could be approximated as two layers, (Cr, Mn) oxide as outer layer and Cr oxide as inner layer (Fig. 15). A clear gradient of Mn was observed across the scale increasing towards gas/alloy interface. The presence of Fe in the outer layer was also observed. As seen in the 500 h specimen, internal oxidation of Ti was observed. As the substrate remains same, microstructure was also same.

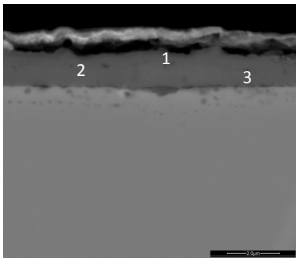

Spectrum	O	Si	Ti	Cr	Mn	Fe	Total (Wt%)
Spectrum 1	60.4	0.5	0.7	24.9	4.9	8.4	100.0
Spectrum 2	53.2	0.6	0.8	39.8	2.3	3.1	100.0
Spectrum 3	38.0	0.8	2.2	46.9	0.6	11.2	100.0

Fig 15: EDS analysis showing the oxide scale composition across the scale of 441 steel exposed for 24 h at 850 °C in Ar-3%H_2-40%H_2O environment

Oxidation was seen to be prominent at the grain boundaries when the surface was observed (Fig. 16). This can be seen as network of oxide along the grain boundaries of the substrate. Discontinuous agglomerates were also observed.

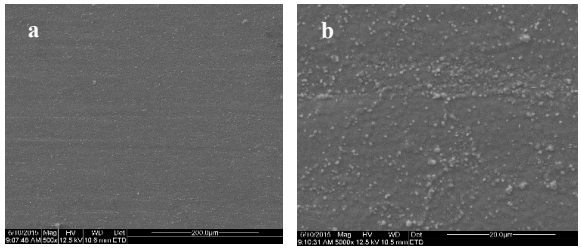

Fig 16: SEM photomicrographs showing the surface of 441 steel exposed for 24 h at 850 °C in Ar-3%H_2-40%H_2O environment (a) lower magnification and (b) higher magnification

Microscopy on the cross section of steel exposed for 500 h at 850 °C revealed dense and adherent oxide scale with whiskers protruding from the scale/gas interface. The oxide scale was assumed to be consisting of two layers; inner layer, which had few pores, and the outer layer with whiskers appeared to be dense (Fig. 17). At the alloy/scale interface, a thin layer of oxide was observed which was discontinuous in

nature. Internal oxidation was also evident from the analysis in the alloy close to alloy/scale interface. Secondary phase particles were found at the grain boundaries in the alloy microstructure. The thickness of the scale was found to be approximately 7 µm.

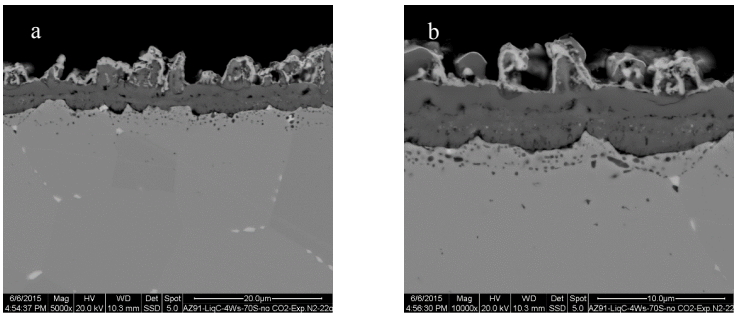

Fig 17: SEM photomicrographs showing the cross section of 441 steel exposed for 500 h at 850 °C in Ar-3%H_2-40%H_2O environment (a) lower magnification and (b) higher magnification

(Fe,Cr) oxide with Mn was observed to have formed in the outer layer while Cr oxide formed the inner layer. The outer layer with Fe was considerably thick (approximately 5 µm). Internal oxidation of titanium was observed beneath the Cr oxide scale at alloy/scale interface (Fig. 18). Second phase particles at the grain boundaries in the alloy are expected to be niobium and silicon based Laves phases [27]. Some crystals on the surface of the steel were rich in Cr whereas the others were rich Fe and the Cr rich crystals also contained Mn (Fig. 19).

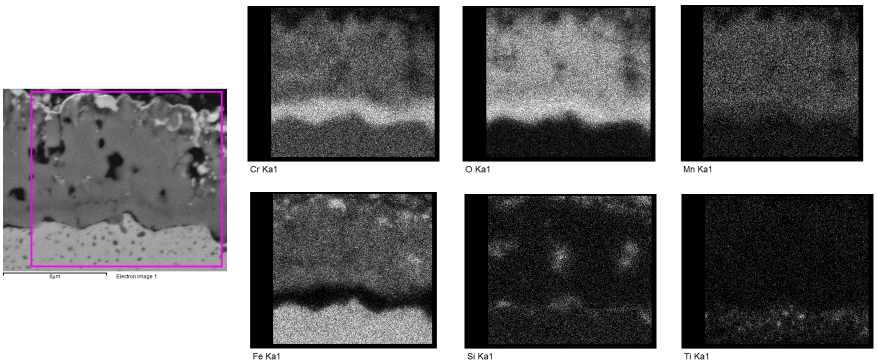

Fig 18: EDS area scan analysis showing the oxide scale composition of 441 steel exposed for 500 h at 850 °C in Ar-3%H_2-40%H_2O environment

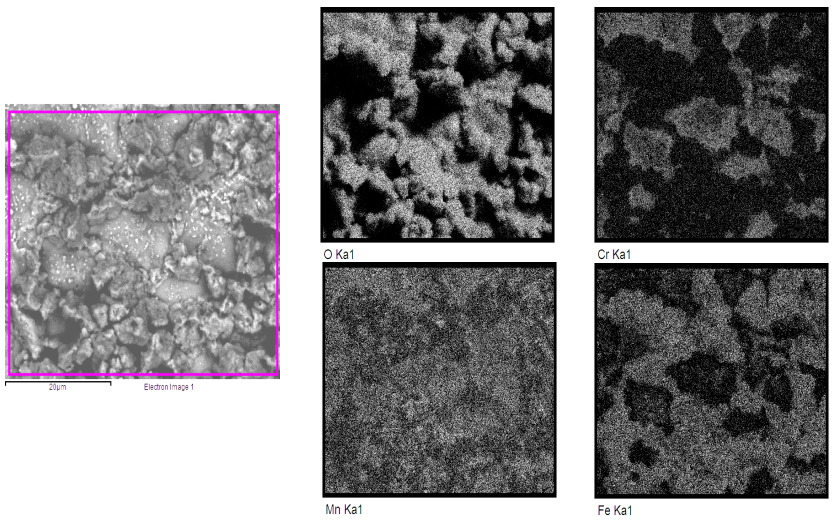

Fig 19: EDS area scan showing the top surface of 441 steel exposed to 850 °C for 500 h in Ar-3%H_2-40%H_2O environment

3.2.1.2 Ar-0.75%H_2-10%H_2O environment

The oxide scale of the steel exposed for 24 h at 850 °C could not be resolved clearly due to experimental reasons. EDS analysis revealed Cr oxide scale though it was difficult to resolve. Oxide surface was observed, which revealed oxidation along the grain boundaries of the substrate (Fig. 20).

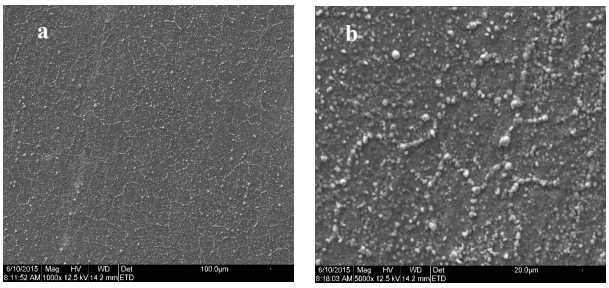

Fig 20: SEM photomicrographs showing the surface of 441 steel exposed for 24 h at 850 °C in Ar-0.75%H_2-10%H_2O environment (a) lower magnification and (b) higher magnification

Micrograph of the steel exposed for 500 h at 850 °C revealed nearly uniform oxide scale with heavy internal oxidation at alloy/scale interface (Fig 21). An absence of pores in the scale and oxidation in the substrate near the alloy/scale interface was also observed. Contact between oxide scale and substrate was poor compared to Ar-3%H_2-40%H_2O environment exposed for 500 h.

Fig 21: SEM photomicrographs showing the cross section of 441 steel exposed for 500 h at 850 °C in Ar-0.75%H_2-10%H_2O environment

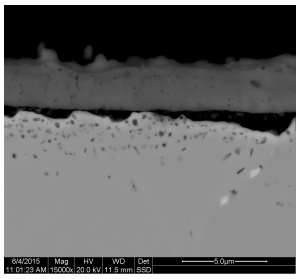

EDS analysis on the cross section revealed an increase in Mn concentration towards the outer layer of the scale making (Cr, Mn) oxide as outer layer and Cr oxide as inner layer (Fig. 22). A slight increase in the concentration of Fe should be noted towards the scale/gas interface. Internal oxide layer of TiO_2 and SiO_2 was also observed. Oxide scale surface morphology revealed oxide crystallites (Fig 23). Thickness of the scale was uniform and approximated to be 3-3.2 μm.

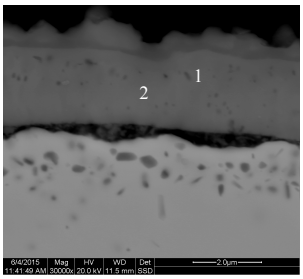

Spectrum	O	Si	Ti	Cr	Mn	Fe	Total (Wt%)
Spectrum 1	40.9	0.0	0.9	50.8	2.6	4.5	100.0
Spectrum 2	37.5	0.2	1.4	58.9	1.1	0.7	100.0

Fig 22: EDS line scan analysis showing the oxide scale composition across the scale of 441 steel exposed for 500 h at 850 °C in Ar-0.75%H_2-10%H_2O environment

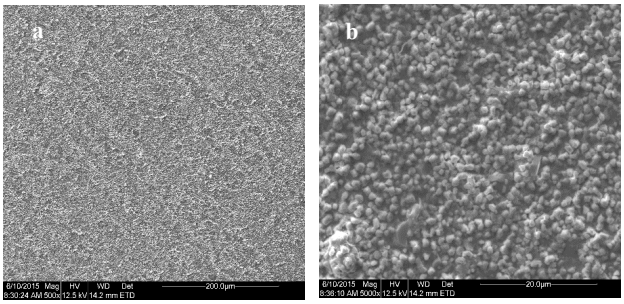

Fig 23: SEM photomicrographs showing the surface of 441 steel exposed for 500 h at 850 °C in Ar-0.75%H_2-10%H_2O environment (a) lower magnification and (b) higher magnification

3.2.2 Crofer 22 Steel

3.2.2.1 Ar-3%H_2-40%H_2O environment

For experimental reasons, sample exposed for 72 h was analyzed instead of 24 h. The oxide scale thickness was observed to be non-uniform and fibrous growth was predominantly seen at scale/gas interface (Fig. 24). Similar to the observations made in 500 h Crofer 22 APU steel sample, inward growth of oxide scale was seen.

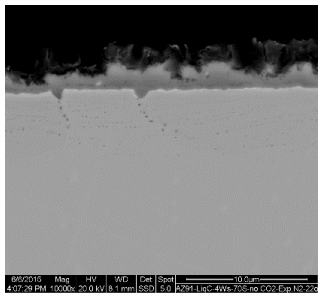

Fig 24: SEM photomicrographs showing the cross section of Crofer 22 APU steel exposed for 72 h at 850 °C in Ar-3%H_2-40%H_2O environment

EDS analysis observations could be approximated to (Cr, Mn) oxide layer and Cr oxide. This observation was similar to that of 500 h sample except for absence of Fe in the outer layer of 72 h sample (Fig. 25). SEM analysis on the surface revealed nucleation of the oxide but did not cover the substrate totally (Fig. 26). Fine whiskers and coarse oxide crystals were observed on the surface of the oxide scale. Thickness of the scale was approximated to be 0.95 to 1.50 µm.

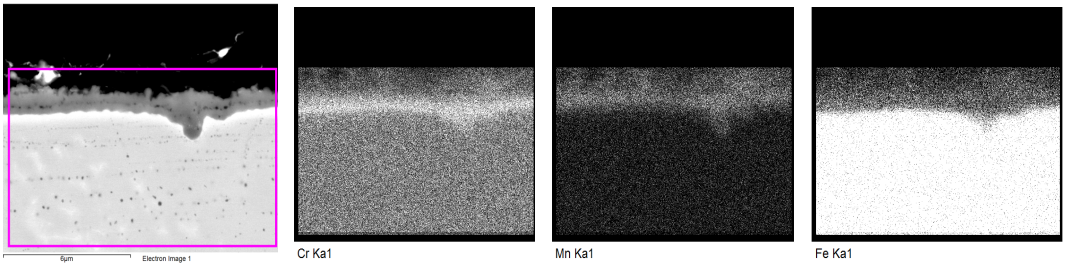

Fig 25: EDS line scan analysis showing the oxide scale of Crofer 22 APU steel exposed for 72 h at 850 °C in Ar-3%H_2-40%H_2O environment

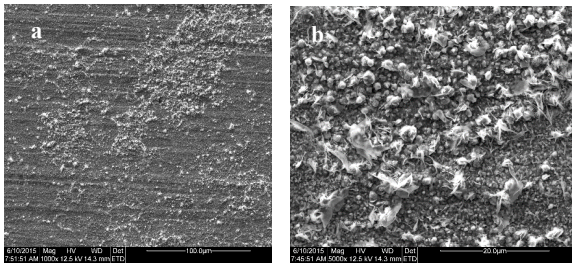

Fig 26: SEM photomicrographs showing the surface of Crofer 22 APU steel exposed for 72 h at 850 °C in Ar-3%H_2-40%H_2O environment (a) lower magnification and (b) higher magnification

Photomicrographs of the cross section of steel exposed for 500 h at 850 °C revealed not so uniform oxide scale with a few pores near alloy/scale interface. Fibrous structure was observed at scale/gas interface (Fig. 27). At a few locations, the oxide scale was observed to be growing into the substrate which shows the occurrence of inward oxide growth. The thickness of the scale was found to be in the range of 2.0 to 2.7 µm. The wide range of thickness was due to inward growth of oxide at few locations.

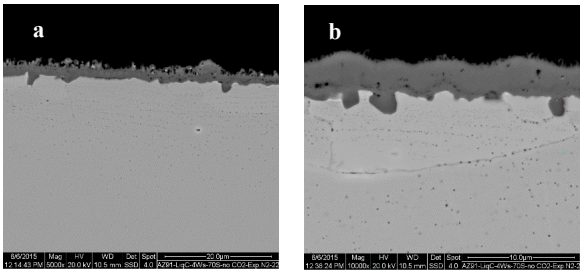

Fig 27: SEM photomicrographs showing the cross section of Crofer 22 APU steel exposed for 500 h at 850 °C in Ar-3%H_2-40%H_2O environment (a) lower magnification and (b) higher magnification

Similar to 441 steel, the above observed oxide scale can be seen as two layers based on EDS analysis. The outer layer was found to be Cr and Mn based oxide with Fe whereas; the inner layer is Cr oxide (Fig. 28). Internal oxidation was also observed in the substrate near alloy/scale interface. SEM on surface of the specimen exposed for 500 h revealed oxide layer completely covering the substrate (Fig. 29). Large crystals were observed at a few locations of which few were rich in Cr and few others in Mn.

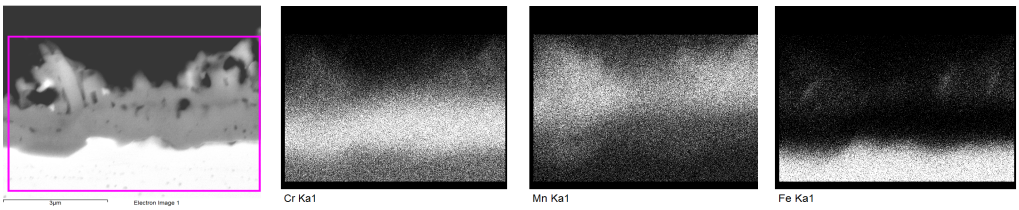

Fig 28: EDS area scan analysis showing the oxide scale composition in Crofer 22 APU steel exposed for 500 h at 850 °C in Ar-3%H_2-40%H_2O environment

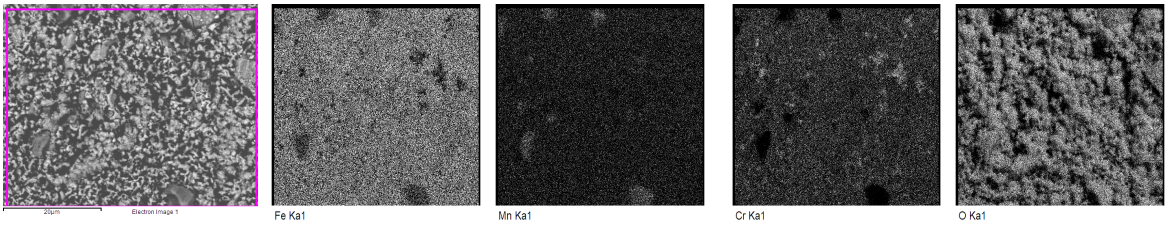

Fig 29: SEM photomicrographs showing the surface of Crofer 22 APU steel exposed for 500 h at 850 °C in Ar-3%H_2-40%H_2O environment

3.2.2.2 Ar-0.75%H_2-10%H_2O environment

Oxide scale of steel exposed for 24 h at 850 °C was observed to be nearly uniform in thickness through the length of the specimen. Inward growth of oxide at the scale-metal interface and fibrous oxide was observed at a few locations (Fig. 30). As the steel under investigation is exposed for 24 h in Ar-0.75%H_2-10%H_2O environment, it cannot be compared to the 72 h specimen in Ar-3%H_2-40%H_2O environment.

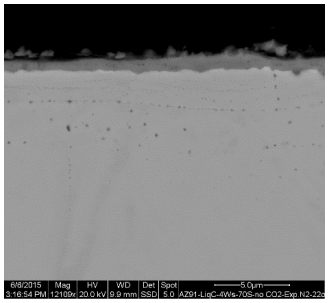

Fig 30: SEM photomicrographs showing the cross section of Crofer 22 APU steel exposed for 24 h at 850 °C in Ar-0.75%H_2-10%H_2O environment

EDS analysis revealed similar two layer oxide structure similar to that of steel exposed to Ar-3%H_2-40%H_2O environment (Fig. 31). Nucleation of the oxide crystals along the grain boundaries was observed

on the surface (Fig. 32). Few locations revealed agglomerates of oxide crystals along grain boundaries. Thickness of the scale is approximated to be around 1.1 to 1.3 µm.

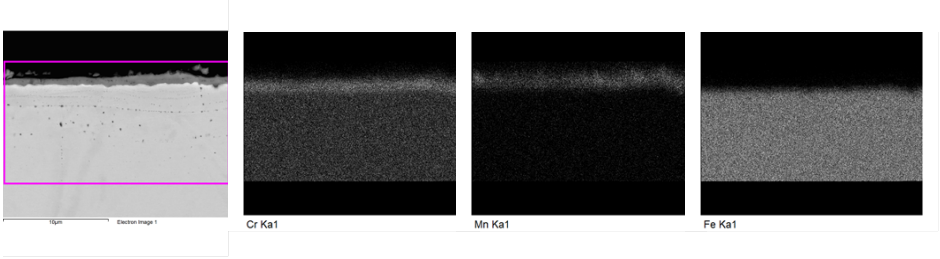

Fig 31: EDS area scan analysis showing the oxide scale composition of Crofer 22 APU steel exposed for 24 h at 850 °C in Ar-0.75%H_2-10%H_2O environment

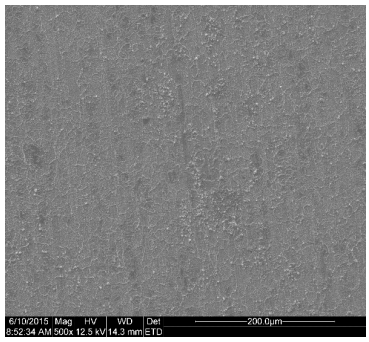

Fig 32: SEM photomicrographs showing the surface of Crofer 22 APU steel exposed for 24 h at 850 °C in Ar-0.75%H_2-10%H_2O environment

Oxide scale of the steel exposed to 850 °C for 500 h revealed to be non-uniform in nature. At few locations, inward growth of oxide was observed. Voids were also observed in an otherwise compact and adherent scale. Similar observations were made in the same steel exposed to 850 °C for 500 h in Ar-3%H_2-40%H_2O environment (Fig. 33). Heavy internal oxidation was observed near the alloy/scale interface.

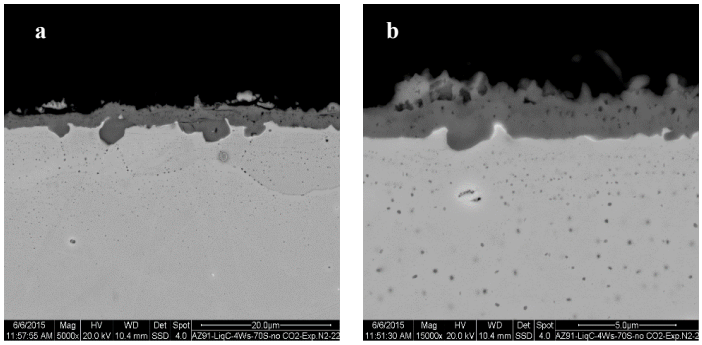

Fig 33: SEM photomicrographs showing the cross section of Crofer 22 APU steel exposed for 500 h at 850 °C in Ar-0.75%H_2-10%H_2O environment (a) lower magnification and (b) higher magnification

EDS analysis showed (Cr, Mn) oxide outer layer and Cr oxide inner layer (Fig. 34). Presence of Fe in the outer layer should be noted. These results are similar to Ar-3%H_2-40%H_2O environment tested Crofer 22 APU steel owing to their similar mass gain. As the scale is non-uniform, the thickness was difficult to approximate. Photomicrographs of the oxide surface indicated continuous oxide scale and discontinuous agglomerates at few locations. Whiskers were seen on the top surface. Cr rich oxide crystals were seen on the oxide scale (Fig. 35).

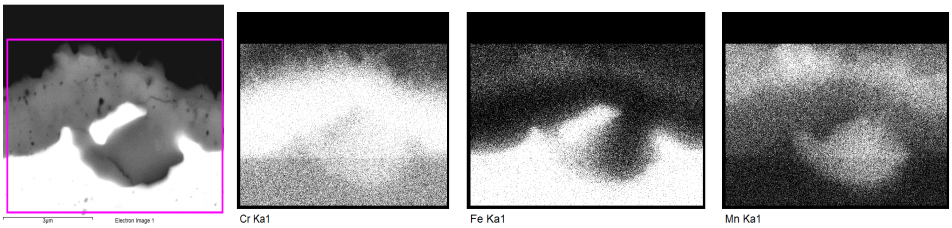

Fig 34: EDS line scan analysis showing the oxide scale composition of Crofer 22 APU steel exposed for 500 h at 850 °C in Ar-0.75%H_2-10%H_2O environment

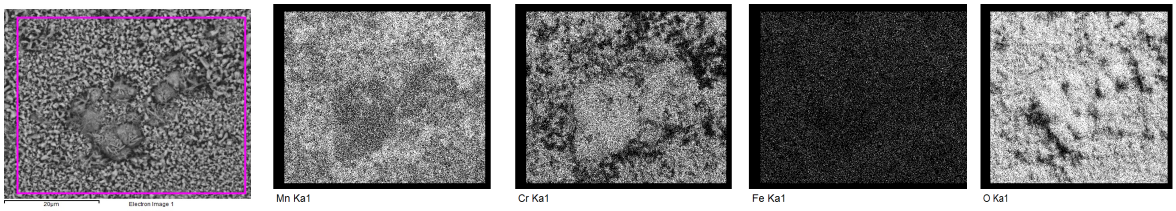

Fig 35: SEM photomicrographs showing the surface of Crofer 22 APU steel exposed for 500 h at 850 °C in Ar-0.75%H_2-10%H_2O environment

3.3 Area Specific Resistance

ASR was evaluated for Crofer 22 APU steel and is plotted in Fig. 36(a). As mentioned in the experimental section, two methods were employed for the specimen preparation to measure ASR. From the first technique a few electrodes (6 nos.) were qualified for measurement whereas from the second technique the number of electrodes (18 nos.) qualified was more compared to the first technique. The resistance was measured from 850 °C to 500 °C and the values were varying from 0.045 to 0.5 Ω cm^2. Activation energy was calculated using the ASR values obtained and substituting them in Eq. 20. Obtained activation energy values are plotted in Fig. 36(b).

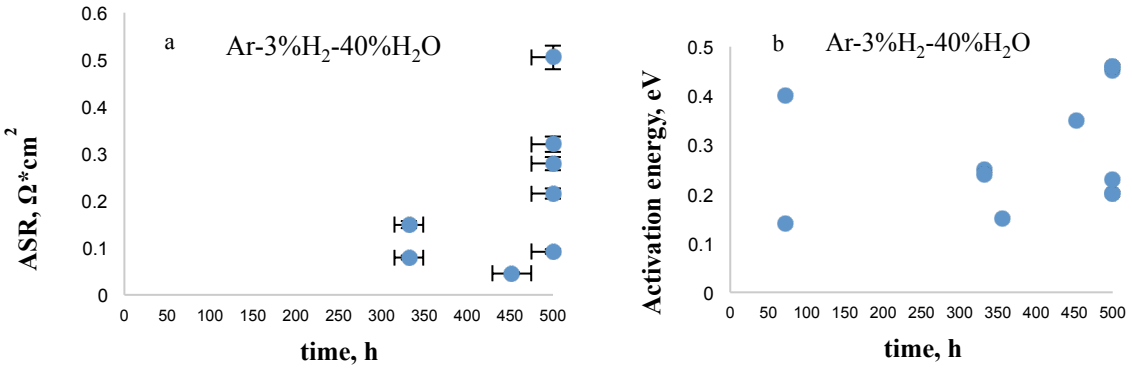

Fig 36: (a) graph showing the plot between ASR and exposure time (b) plot between activation energy and exposure time

4 DISCUSSION

In the present study, when 441 steel and Crofer 22 APU steel were exposed to same conditions, the effect of dilution of environment was observed only in the case of 441 steel. In Ar-3%H_2-40%H_2O environment, the rate of mass gain for 441 steel was measured to be highest after 500 h of exposure at 850 °C. A decrease in the rate of mass gain was observed when the Ar-3%H_2-40%H_2O environment was diluted using Ar to Ar-1.5%H_2-20%H_2O and Ar-0.75%H_2-10%H_2O (Fig. 10). There was a deviation from the parabolic growth rate for 441 steel in Ar-3%H_2-40%H_2O environment (Fig. 12). Cross-sectional analysis of a 441 sample exposed in this particular environment for 500 h revealed a thick oxide, which was rich in Fe (Fig. 17-18). Interestingly, Fe was present in the oxide scale from the initial hours of oxidation, as seen from the sample exposed for 24 h (Fig. 14&15). Diffusion of Fe from the substrate to the oxide scale increased with increasing hours of exposure, which contributed to the elevated mass gain in 441 steel in the high moisture content environment, compared to the exposure in lower moisture concentration. In Ar-1.5%H_2-20%H_2O and Ar-0.75%H_2-10%H_2O environments, the oxidation rate, measured by mass gain, was observed to be approximately 0.50 mg/cm^2 and followed parabolic growth rate (as seen in Fig. 10&12). This is likely due to the more protective scale formed in 441 steel in the diluted environments, but not in the case of Ar-3%H_2-40%H_2O environment. In the case of Crofer 22 APU steel, the average mass gain in all the three environments examined had a similar value (approximately 0.47 mg/cm^2), i.e. dilution of the environment had no effect on the oxidation rate of Crofer 22 APU steel. Oxide scales formed on Crofer 22 APU steel were similar to those of 441 steel in Ar-1.5%H_2-20%H_2O and Ar-0.75%H_2-10%H_2O environments, with a dense chromia layer in contact with the steel interface. Though pO_2 remained constant in all the environments, difference in total pressure of H_2O and H_2 influenced the oxidation behavior of 441 steel in Ar-3%H_2-40%H_2O environment. No influence was observed in Crofer 22 APU steel. Lower amount of Cr in 441 steel (18% Cr) compared to 22% Cr and presence of reactive elements in Crofer 22 APU steel might have contributed to the difference in oxidation behavior between the steels.

The oxide scale in 441 steel can be assumed to consist of two layers, though the individual layers could not be clearly be distinguished by microscopy except in Ar-3%H_2-40%H_2O environment exposed for 500 h. The inner layer consisted of chromia while the outer layer consisted of Cr and Mn. Fe was present only in the outer layer when the steel was exposed for 500h in Ar-1.5%H_2-20%H_2O and Ar-0.75%H_2-10%H_2O environments. But when exposed for only 24 h in Ar-3%H_2-40%H_2O environment, it revealed Fe in the outer layer, which led to the higher mass gain. An oxidation model for 441 steel showing the suggested formation of the oxide scale is given in Fig 37. The scale composition observed by Ardigo, et al [38] in 441 steel when exposed to low pO_2 environment was similar to the scale formed on 441 steel in the present study, which was chromia as inner scale and (Cr, Mn) oxide with Fe as an outer scale. Ardigo et al [38] observed TiO_2 in 441 steel at the scale/alloy interface, which is also similar to the observations made in the present case of 441 steel. According to thermodynamics, TiO_2 must be present on the outer layer of the scale but is found to be at the interface between scale and alloy due to its high oxygen affinity [39]. This can be because the pO_2 below chromia scale is sufficient to internally oxidize Ti before it reaches the surface.

Even in the case of Crofer 22 APU steel the oxide scale was observed to consist of two layers similar to that of 441 steel. This kind of scale is typical to all Mn containing steels which form a protective chromia layer. The presence of Fe in the outer layer of the scale was observed after 500 h exposure but the it's concentration was lower when compared to 441 steel in Ar-3%H_2-40%H_2O environment. In Ar-1.5%H_2-20%H_2O and Ar-0.75%H_2-10%H_2O environments, Fe concentration in the outer layer of Crofer 22 APU steel was found to be similar to that of 441 steel after 500 h. Mn and Fe ions diffuse from the substrate, through the formed chromia scale during longer exposure hours forming an outer layer rich in Cr and Mn oxide with some Fe. A suggested oxidation model for Crofer 22 APU steel, showing the oxide scale formation in the studied environments, is given in Fig 38. Young, et al, studied the oxidation behavior of Crofer 22 APU steel in low pO_2 environment in the temperature range of 550 °C-800 °C [39]. They observed the presence of Fe_3O_4 in the outer layer and $(Fe,Cr,Mn)_3O_4$ as sub layer and a passivated Cr_2O_3 layer at a few locations in the samples treated at 650 °C for 500 h in Ar-4% H_2-20%H_2O environment. In their study, when the same steel was exposed to 800 °C in the same environment for 500 h, it revealed $MnCr_2O_4$ layer with Cr_2O_3 layer [40]. But in the present case, Crofer 22 APU steel revealed Fe as well apart from Cr, Mn in the outer layer of the scale after being exposed for 500 h at 850 °C in both Ar-3%H_2-40%H_2O and Ar-0.75%H_2-10%H_2O environments.

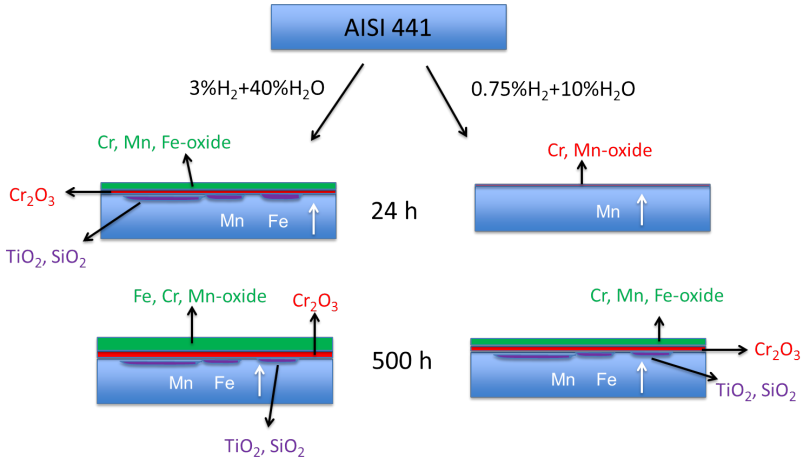

Fig 37: Oxidation model of AISI 441 steel exposed to Ar-3%H_2-40%H_2O and Ar-0.75%H_2-10%H_2O environments

Since Fe is present in the oxide scales of both the steel samples exposed for longer times and higher moisture content, there might be an influence of moisture content in the environment on Fe diffusion from substrate to the scale. According to Larring, et al [40] dissolution of protons from water vapor increases the solubility and diffusivity of iron in the chromia scale, which affects the oxidation behavior. This explains the above assumption of higher concentration of Fe in the outer scale of specimens exposed in Ar-3%H_2-40%H_2O environment compared to Ar-0.75%H_2-10%H_2O environment in the case of 441 steel. In the case of Crofer 22 APU steel, the presence of Fe was observed in all the three environments when exposed for longer hours. Researchers like Zheng, Young & Heuer observed the mechanism of oxygen containing species diffusing through the Fe oxide scale to form inward growing chromia scale. They have also observed OH°_{o} to be a major point defect in scale responsible for the oxide scale growth [41]. As the oxygen containing species travel through the scale, they react with Cr ions forming inward growing oxide scale (as evident form the morphology of the scale in Crofer 22 APU steel). Through the diffusion paths of already formed chromia scale, Mn^{2+} can diffuse and form (Cr,Mn) oxide. When FeCr steels are exposed to high pO_2 environments, oxide scale growth is generally considered to be predominantly outwards [42].

The composition gradient observed across the oxide scale (in both the steels) reflects the permeability of chromia scale to elements like Mn and Fe. Naoumidis, et al, reported rapid transport of Mn through Cr_2O_3 to form an outer spinel layer in heat resisting steels. Researchers found similar results when FeCr steels were tested in low pO_2 environments [43]. Stygar, et al, observed a layer of (Cr, Mn) oxide layer on top of the chromia scales [44]. This was explained to be due to the fast diffusion of Mn along the ferrite and chromia grain boundaries compared to Cr^{3+}. This is consistent with the report by Cox, et al, who showed that the diffusivities of metal ions in Cr_2O_3 decrease in the order D_{Mn}, D_{Fe}, D_{Ni} and D_{Cr}, assuming metals diffuse as ions via Cr^{3+} lattice sites in Cr_2O_3 [45].

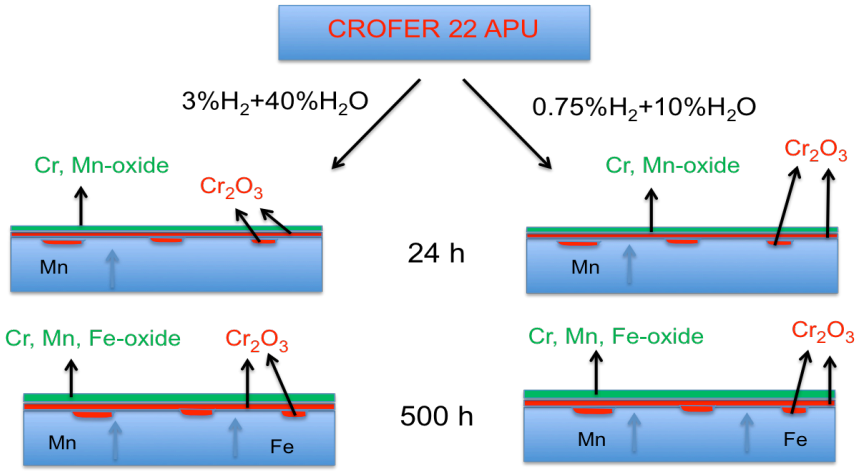

Fig 38: Oxidation model of Crofer 22 APU steel exposed to Ar-3%H_2-40%H_2O and Ar-0.75%H_2-10%H_2O environments

The oxide scale morphology is also very important since the scale growth proceeds through solid-state diffusion as seen by parabolic growth rate. Researchers like Zurek et al, stated that oxides grown in low pO_2 environments develops fine-grained scale and the scale growth proceeds through inward diffusion of oxygen through the grain boundaries of the scale. They used oxygen tracers to prove that scale grown in Ar-O_2 (high pO_2) was by nearly outward cation diffusion whereas low pO_2 indicated scale growth nearly by inward transport via diffusion paths. It was also reported that the scale was adherent and compact in low pO_2 environment whereas high pO_2 environment revealed voids and internal pores at oxide-alloy interface [46]. Decrease in porosity at the scale/metal was also observed in low pO_2 environment, which is attributed to presence of water vapor [43]. Even in present study (low pO_2) oxide scale in both the steels, revealed adherent and compact scale with a few voids. It was proposed that the less voidage observed in the scale grown in low pO_2 environment is due to the H_2O/H_2 bridges in the voids which prevent vacancy condensation and void growth otherwise present in high pO_2 environment [20]. In simpler terms, water vapor provides rapid gas transport of oxygen from the pore, which otherwise continues to be present in the pore space in high pO_2 environment [46]. Other observation made in the present study was the absence of spallation. Generally, rare earth elements are added to avoid spallation. In the present case, La was present in Crofer 22 APU steel whereas 441 steel was devoid of any rare elements but still exhibited an adherent scale.

Whisker formation was observed in the present study for both steels (as seen in Fig. 17, 24, 27, 30&33), whose formation is encouraged by the presence of water vapor. This is suggested to be because the water vapor induces plasticity to the scale which is important for thermal cycling and also favors formation of fine grains in the scale [47]. Stygar. et al, observed whiskers at the scale/gas interface and fine crystalline structure at the scale/alloy interface in FeCr steel exposed to Ar-H_2-H_2O environment. Whisker morphology was similar to what was seen in both the steels in the present study. These whiskers, grown on the outer surface of the scale are less protective in nature whose formation is encouraged by presence of water vapor [44].

4.1 Area Specific Resistance

ASR values obtained in the present study were spread over a range of magnitude. ASR parameter varied from 0.04 to 0.5 Ω cm^2, lowest being 0,045 Ω cm^2 for samples exposed for 452 h. Obtained values for ASR were very high as literature about interconnect conductivity in SOFC showed that 0.1 Ω cm^2 is the maximum permissible value of ASR for the cell to function properly during its life time [4].

Ardigo et. al, found ASR values for Crofer 22 APU steel to be above the permissible limit of 0.1 Ω cm^2 when measured in Ar-1%H_2-5.6%H_2O environment at 800 °C [49]. This is in agreement with the present case as most of the values were above 0.1 Ω cm^2. Few researchers proposed that presence of dissolved hydrogen modifies the oxide electrical properties, which affect the conductivity adversely [50, 51]. Guilou et. al, calculated ASR of Alloy 230 (composition of Alloy 230 is near to Crofer 22 APU steel in terms of Cr and Mn content) in both high pO_2 and low pO_2 conditions. They observed that ASR in low pO_2 environment was at least one order higher in magnitude compared to ASR values obtained from high pO_2 environment and was attributed to presence of hydrogen in low pO_2 environment [52].

In the present case, inconsistency in the measured values may be due to problems in electrode preparation or due to contact problems during measurement. It is difficult to point out the exact reason for the scatter. This scatter of values makes it difficult to know the exact value of electrical conductivity but the values were above the permissible limit of 0.1 Ω cm^2. Activation energy expression (Eq. 20) shows how conductivity of oxide scale is temperature dependent and it also supports that an oxide measured was semiconductor. As ASR values were scattered and higher than the permissible limit, the corresponding activation energy values were also scattered and low.

5 CONCLUSIONS

- The present study was aimed to investigate the effect of dilution of environment on oxidation behavior of 441 steel and Crofer 22 APU steel. This was studied by varying the amounts of water vapor and hydrogen in low pO_2 atmosphere. Ar-3%H_2-40%H_2O, Ar-1.5%H_2-20%H_2O and Ar-0.75%H_2-10%H_2O environments were employed to study the behavior. These steels were exposed to 850 °C for up to 500 h.
- pO_2 was kept constant while varying the partial pressures of hydrogen and water vapor. 441 steel showed difference in oxidation behavior on dilution whereas Crofer 22 APU steel remained stable.
- 441 steel also showed parabolic rate growth in all environments except in the case where steel was exposed for 500h in Ar-3%H_2-40%H_2O environment. This deviation from the parabolic rate growth was observed from the initial stages of oxidation as it was rapid in nature. Crofer 22 APU steel showed parabolic rate growth in all the environments.
- The oxide scales that formed were adherent and compact with no spallation for both the materials in all environments.
- Microstructure studies of the cross-section revealed (Cr, Mn) oxide as outer layer with increasing Mn gradient towards the gas/alloy interface and chromia as an inner layer. Presence of Fe was observed near the gas/alloy interface in the steels exposed for 500 h.
- In the case of 441 steel, in Ar-3%H_2-40%H_2O environment concentration of Fe was high in the outer scale after 500 h. Ti oxide and Si oxide layer was observed in 441 steel at scale/alloy interface.
- Higher water vapour content encourages Fe ions diffusion as evident from the EDS analysis of Ar-3%H_2-40%H_2O samples. Mn diffusion through chromia scale was observed in all the cases.
- Attempts were made to measure ASR of Crofer 22 APU steel. Different electrode preparation techniques were tried. Measured ASR values were high compared to that of the targeted value of interconnects. Reasons for deviation from expected values are not known.

ACKNOWLEDGEMENTS

Firstly, I would like to express my gratitude to my supervisors Patrik Alnegren and Jan Gustav Grolig for their useful comments, remarks and engagement through the learning process of this master thesis. I would also like to thank Jan Froitzheim for introducing me to the topic and also for giving an opportunity to carry out the thesis work. Furthermore, I would like to thank Prof. Jan-Erik Svensson for being my examiner. Thanks to Sandra for all the administrative help and Esa Vaäänänen for the support. I would like to thank my friends, who made me feel home in a new country. I owe more than thanks to my family members for their constant support and encouragement throughout my life. Special thanks to my husband, Seshendra, for supporting and inspiring me.

REFERENCES

[1] S. Singhal, “Science and technology of solid-oxide fuel cells,” *MRS Bull.*, vol. 25, no. 3, pp. 16–21, 2000.

[2] E. S. Assocation, “No Title,” *http://energystorage.org/energy-storage/technologies/hydrogen-energy-storage*. .

[3] M. A. Laguna-Bercero, “Recent advances in high temperature electrolysis using solid oxide fuel cells: A review,” *J. Power Sources*, vol. 203, pp. 4–16, Apr. 2012.

[4] W. Zhu and S. Deevi, “Opportunity of metallic interconnects for solid oxide fuel cells: a status on contact resistance,” *Mater. Res. Bull.*, 2003.

[5] “Electrolysis:Obtaining hydrogen from water: The Basis for a Solar-Hydrogen Economy,” *http://www.nmsea.org/Curriculum/7_12/electrolysis/electrolysis.htm*. .

[6] “No Title,” *http://www.meritnation.com/ask-answer/question/explain-the-electrolysis-of-water-with-the-help-of-a-well-la/science/3571089*. .

[7] J. McMurry and R. Fay, “Chemistry (ed.),” in *Electrochemistry in Chemistry*, 2001.

[8] S. H. Jensen, P. H. Larsen, and M. Mogensen, “Hydrogen and synthetic fuel production from renewable energy sources,” *Int. J. Hydrogen Energy*, vol. 32, no. 15, pp. 3253–3257, Oct. 2007.

[9] W. DONITZ, “High-temperature electrolysis of water vapor?status of development and perspectives for application,” *Int. J. Hydrogen Energy*, vol. 10, no. 5, pp. 291–295, 1985.

[10] S. Elangovan, J. H. (2001). Planar solid oxide fuel cell development at SOFCs. In S. S. H. Yokokawa (Ed.), *Proceedings of the Seventh International Symposium on Solid Oxide Cells. (SOFC-VII)*, pp. 94-99. Pennington, NJ: The Electrochemical Society.

[10] K. Foger, R. D. (October 17-22, 1999). (SOFC-VI). In M. D. S.C. Singhal (Ed.), *Proceedings of the Sixth International Symposium on Solid Oxide Fuel Cells* (p. 95). Honolulu, Hawaii: SOFC.

[11] http://www.aki.che.tohoku.ac.jp/~koyama/html/research/SOFC.html.

[12] N. Q. Minh, “Ceramic Fuel Cells,” *J. Am. Ceram. Soc.*, vol. 76, no. 3, pp. 563–588, Mar. 1993.

[13] X. Cao and H. Zhang, “Development of Solid Oxide Electrolyzer Cell (SOEC) Cathode Materials,” *Adv. Mater. Res.*, 2012.

[14] K. SUN, J. PIAO, N. ZHANG, X. CHEN, S. XU, and D. ZHOU, “Fabrication and performance of La0.8Sr0.2MnO3/YSZ graded composite cathodes for SOFC,” *Rare Met.*, vol. 27, no. 3, pp. 278–281, Jun. 2008.

[15] N. Minh, “Ceramic fuel cells,” *J. Am. Ceram. Soc.*, 1993.

[16] H. Tsuneizumi, “Development of Solid Oxide Fuel Cell With Metallic Separator,” *Int. Fuel Cell Conf. Proceedings. ...*, 1992.

[17] K. Foger, R. D. (October 17-22, 1999). (SOFC-VI). In M. D. S.C. Singhal (Ed.), *Proceedings of the Sixth International Symposium on Solid Oxide Fuel Cells* (p. 95). Honolulu, Hawaii: SOFC.

[18] J. Wu and X. Liu, “Recent Development of SOFC Metallic Interconnect,” *J. Mater. Sci. Technol.*, vol. 26, no. 4, pp. 293–305, Apr. 2010.

[19] Yang, Zhenguo, et al. "Electrical contacts between cathodes and metallic interconnects in solid oxide fuel cells." *Journal of Power Sources* 155.2 (2006): 246-252.

[20] W. Quadakkers, “Metallic interconnectors for solid oxide fuel cells–a review,” *Mater. high ...*, 2003.

[21] J. Froitzheim and H. Ravash, “Investigation of chromium volatilization from FeCr interconnects by a denuder technique,” *J. ...*, 2010.

[22] X. Chen, P. Hou, and C. Jacobson, “Protective coating on stainless steel interconnect for SOFCs: oxidation kinetics and electrical properties,” *Solid State Ionics*, 2005.

[23] D. Jones, “Principles and prevention of corrosion,” 1992.

[24] P. Kofstad, “High temperature corrosion,” *Elsevier Appl. Sci. Publ. Crown House, ...*, 1988.

[25] S. Ebbesen and M. Mogensen, “Electrolysis of carbon dioxide in solid oxide electrolysis cells,” *J. Power Sources*, 2009.

[26] “http://oregonstate.edu/instruct/me581/Exams/F10/ME581F10Final.html.” .

[27] Grolig, Jan Gustav. "Coated Ferritic Stainless Steels as Interconnects in Solid Oxide Fuel Cells." (2013).

[28] S. Fontana, R. Amendola, and S. Chevalier, “Metallic interconnects for SOFC: Characterisation of corrosion resistance and conductivity evaluation at operating temperature of differently coated alloys,” *J. Power ...*, 2007.

[29] J. Grolig, J. Froitzheim, and J. Svensson, “Coated stainless steel 441 as interconnect material for solid oxide fuel cells: Evolution of electrical properties,” *J. Power Sources*, 2015.

[30] J. Fergus, “Materials challenges for solid-oxide fuel cells,” *Jom*, 2007.

[31] M. Limooei, “Evaluation of electrical resistance activation energy for cobalt-coated interconnects,” *INDIAN J. ...*, 2013.

[32] “ASR evaluation of different kinds of coatings on a ferritic stainless steel as SOFC interconnects,” *... Coatings Technol.*, 2007.

[33] K. Huang, P. Hou, and J. Goodenough, “Characterization of iron-based alloy interconnects for reduced temperature solid oxide fuel cells,” *Solid State Ionics*, 2000.

[34] H. Asteman, J. Svensson, and L. Johansson, “Evidence for chromium evaporation influencing the oxidation of 304L: the effect of temperature and flow rate,” *Oxid. Met.*, 2002.

[35] S. Jiang and X. Chen, “Chromium deposition and poisoning of cathodes of solid oxide fuel cells–a review,” *Int. J. Hydrogen Energy*, 2014.

[36] A. Petric and H. Ling, “Electrical conductivity and thermal expansion of spinels at elevated temperatures,” *J. Am. Ceram. Soc.*, 2007.

[37] http://www.microscopyu.com/articles/formulas/formulasresolution.html

[38] Ardigo, Maria Rosa, et al. "Optimisation of metallic interconnects for hydrogen production by high temperature water vapour electrolysis." *Defect and Diffusion Forum*. Vol. 323. 2012.

[39] Young, D. J., et al. "Temperature dependence of oxide scale formation on high-Cr ferritic steels in Ar–H 2–H 2 O." *Corrosion Science* 53.6 (2011): 2131-2141.

[40] Larring, Yngve, Reidar Haugsrud, and Truls Norby. "HT Corrosion of a Cr-5 wt% Fe-1 wt% Y_2 O_3 Alloy and Conductivity of the Oxide Scale Effects of Water Vapor." *Journal of the Electrochemical Society* 150.8 (2003): B374-B379.

[41] Zheng, X. G., and D. J. Young. "High-temperature corrosion of Cr2O3-forming alloys in CO-CO2-N2 atmospheres." *Oxidation of Metals* 42.3-4 (1994): 163-190.

[42] Heuer, A. H. "Oxygen and aluminum diffusion in α-Al 2 O 3: How much do we really understand?." *Journal of the European Ceramic Society* 28.7 (2008): 1495-1507.

[43] Naoumidis, A., et al. "Phase studies in the chromium-manganese-titanium oxide system at different oxygen partial pressures." *Journal of the European Ceramic Society* 7.1 (1991): 55-63.

[44] Stygar, Mirosław, et al. "Oxidation properties of ferritic stainless steel in dual Ar–H_2–H_2O/air atmosphere exposure with regard to SOFC interconnect application." *Solid State Ionics* 262 (2014): 449-453.

[45] M.G.E. Cox, B. McEnaney, V.D. Scott. *Phil. Mag*., 26 (1972), p. 839

[46] Zurek, J., et al. "Growth and adherence of chromia based surface scales on Ni-base alloys in high- and low-pO 2 gases." *Materials Science and Engineering: A* 477.1 (2008): 259-270.

[47] Saunders, S. R. J., M. Monteiro, and F. Rizzo. "The oxidation behaviour of metals and alloys at high temperatures in atmospheres containing water vapour: A review." *Progress in Materials Science* 53.5 (2008): 775-837.

[48] Hänsel, M., W. J. Quadakkers, and D. J. Young. "Role of water vapor in chromia-scale growth at low oxygen partial pressure." *Oxidation of Metals* 59.3-4 (2003): 285-301.

[49] Ardigo, M. R., et al. "Evaluation of a new Cr-free alloy as interconnect material for hydrogen production by high temperature water vapour electrolysis: Study in cathode atmosphere." *international journal of hydrogen energy* 37.10 (2012): 8177-8184.

[50] Holt, Arve, and Per Kofstad. "Electrical conductivity and defect structure of Cr 2 O 3. II. Reduced temperatures (<∼ 1000° C)." *Solid State Ionics* 69.2 (1994): 137-143.

[51] Holt, Arve, and Per Kofstad. "Electrical conductivity and defect structure of Mg-doped Cr 2 O 3." *Solid State Ionics* 100.3 (1997): 201-209.

[52] Guillou, S., C. Desgranges, and S. Chevalier. "Influence of a Coating on Oxidation Resistance and Resistivity of a Chromia Former Alloy for High Temperature Vapor Electrolysis Application." *Oxidation of metals* 80.3-4 (2013): 341-361